# Computer Techniques for Planning and Management of OTH Radars

D. L. LUCAS AND J. L. LLOYD

*U.S. Department of Commerce*
*Office of Telecommunications, ITS*
*Boulder, Colorado*

J. M. HEADRICK AND J. F. THOMASON

*Radar Division*
*Naval Research Laboratory*
*Washington, D.C.*



September 1972



**NAVAL RESEARCH LABORATORY**
**Washington, D.C.**



37

UNCLASSIFIED

Security Classification

**DOCUMENT CONTROL DATA - R & D**

*(Security classification of title, body of abstract and indexing annotation must be entered when the overall report is classified)*

1. ORIGINATING ACTIVITY *(Corporate author)*
Naval Research Laboratory
Washington, D.C. 20390

2a. REPORT SECURITY CLASSIFICATION
UNCLASSIFIED

2b. GROUP
---

3. REPORT TITLE

COMPUTER TECHNIQUES FOR PLANNING AND MANAGEMENT OF OTH RADARS

4. DESCRIPTIVE NOTES *(Type of report and inclusive dates)*
An interim report on a continuing problem.

5. AUTHOR(S) *(First name, middle initial, last name)*

James M. Headrick, Joseph F. Thomason, Donald L. Lucas and J. L. Lloyd

| 6. REPORT DATE | 7a. TOTAL NO. OF PAGES | 7b. NO. OF REFS |
|---|---|---|
| September 1972 | 38 | 13 |

| 8a. CONTRACT OR GRANT NO. | 9a. ORIGINATOR'S REPORT NUMBER(S) |
|---|---|
| NRL Problem 53R02-70 | |
| b. PROJECT NO. | NRL Memorandum Report 2500 |
| USAF MIPR FY76207200005 | |
| c. | 9b. OTHER REPORT NO(S) *(Any other numbers that may be assigned this report)* |
| d. | |

10. DISTRIBUTION STATEMENT

Approved for public release; distribution unlimited.

| 11. SUPPLEMENTARY NOTES | 12. SPONSORING MILITARY ACTIVITY |
|---|---|
| | Electronic Systems Division<br>L. G Hanscom Field<br>Bedford, Mass. 01730 |

13. ABSTRACT

Techniques are described for the prediction and analysis of OTH radar operation. A complete ionospheric description is included and optimal computer techniques are utilized to give a practical means to handle the frequency- and antenna-scan management of the radar. Actual data are analyzed to show how the backscatter response from one frequency radar sounding can be used to derive the actual transmission-path characteristics that need to be known for effective radar operation.

12

DD FORM 1 NOV 68 1473 (PAGE 1)

S/N 0101-807-6801

35

UNCLASSIFIED

Security Classification

| 14. KEY WORDS | LINK A | | LINK B | | LINK C | |
|---|---|---|---|---|---|---|
| | ROLE | WT | ROLE | WT | ROLE | WT |
| HF propagation<br>Ionospheric model<br>OTH radars | | | | | | |

## ABSTRACT

Techniques are described for the prediction and analysis of OTH radar operation. A complete ionospheric description is included and optimal computer techniques are utilized to give a practical means to handle the frequency- and antenna-scan management of the radar. Actual data are analyzed to show how the backscatter response from one frequency radar sounding can be used to derive the actual transmission-path characteristics that need to be known for effective radar operation.



## AUTHORIZATION

NRL Problem R02-70

USAF MIPR FY76207200005

## I INTRODUCTION

The Institute for Telecommunication Sciences--Naval Research Laboratory (ITS-NRL) area-coverage model has been developed to serve three purposes--first, the analysis of measured area coverage and radar backscatter data; second, the prediction of the performance of communication and radar systems; and third, as a tool to be used in frequency and scan management of OTH radar systems. The development and use of this model for these purposes have been discussed in many previous reports.[1-3]

The purpose of this paper is to describe the present status of the model and to illustrate its use in analyzing radar backscatter data.

## II MODEL DESCRIPTION

The model is divided into two parts; the first half provides a description of the ionosphere along any look direction of a radar, given its location (Figure 1). If ionospheric data are already available

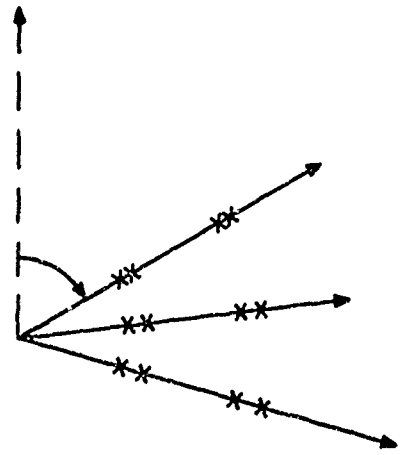

A. At each time (month, UT)
1. Read data tape
2. Reduce time variation

B. At each azimuth
1. Find geometric parameters (latitude, longitude, etc.)
2. Ionospheric indices

C. At each frequency
1. Find radar return (area coverage)

FIGURE 1 MODEL AREA COVERAGE

either from previous analysis or measurement, the first half of the program may be skipped and the data entered directly into the second half of the model (see below for details) If no data are available, the ITS world maps of ionospheric indices are used to generate the description of the ionosphere.[4-9] These maps have been in use several years except for the F1-layer, which is described in detail in Ref. 9 and summarized in the Appendix. The ionosphere is described initially by four ionized regions--the regular E, the F1 if present, the F2, and the sporadic E.

The E, F1, and F2 are described each by four indices--the critical frequency, the height of maximum ionization, the semi-thickness of the layer, and an absorption factor (described in detail below, it corresponds roughly to the averaged effect of the product of collision frequency and electron density). The sporadic E is described by four parameters--the height of reflection, the lower decile, the median, and the upper decile value of median critical frequency. These sixteen indices form the first rough description of the ionosphere; if desired these may be entered as input data rather than generated from the world maps.

The second step of the model is to generate an electron-density profile describing the E, F1, and F2 portions of the ionosphere. At each selected height the square of the plasma frequency is generated using the equations for a parabolic layer (Figure 2):

$$f_N^2 = f_c^2\left[1 - \left(\frac{h-h_m}{y}\right)^2\right] \qquad (1)$$

where

$f_c$ = Critical frequency

$h_m$ = Height of maximum ionization

$y$ = Semi-thickness of the layer

$h$ = Height (usually every 2 km) for which the plasma frequency $f_N$ is calculated.

The layers may, of course, overlap, and the maximum $f_N^2$ for the three layers is used. Normally the virtual height of the E layer

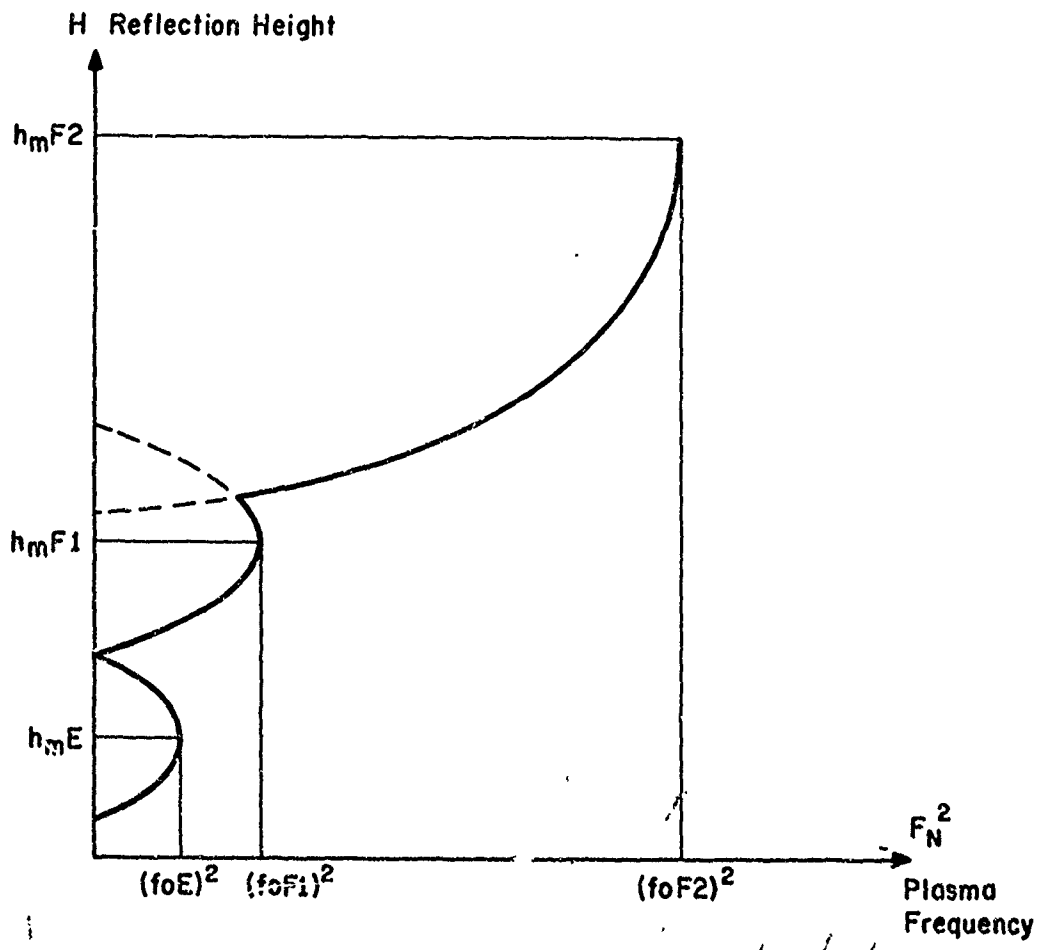


FIGURE 2 INITIAL DESCRIPTION OF THE IONOSPHERE

(approximately 110 km) is used to start the electron-density profile at the bottom. This yields virtual-height ionograms and raypaths that agree well with measured data. If desired, an option exists to tail off the E layer with a linear layer down to a desired level. For example, if the bottom of the E layer is taken to be 90 km, a linear tail to the E layer starting at 100 km and extending down to 70 km will produce a virtual height of 110 km at a true height of 110 km [$f_N^2 = 0.75(f_o E)^2$ for a semithickness of 20 km]. Again, it is optional to enter any electron-density profile desired.[10]

The fourth step of the model is to generate a virtual-height ionogram from the electron-density profile (Figure 3). Here a numerical integration is used to evaluate the virtual height, h′:

$$h' = \int_{h_o}^{h_r} \mu'(h)\,dH$$

$$\mu' = \frac{1}{\sqrt{1 - y^2}}$$

$$y^2 = \frac{f_N^2}{f_c^2} \qquad (2)$$

where

$\mu'$ = Group index of refraction

$y$ = Ratio of plasma frequency to critical frequency

$h$ = Height corresponding to $f_N^2$.

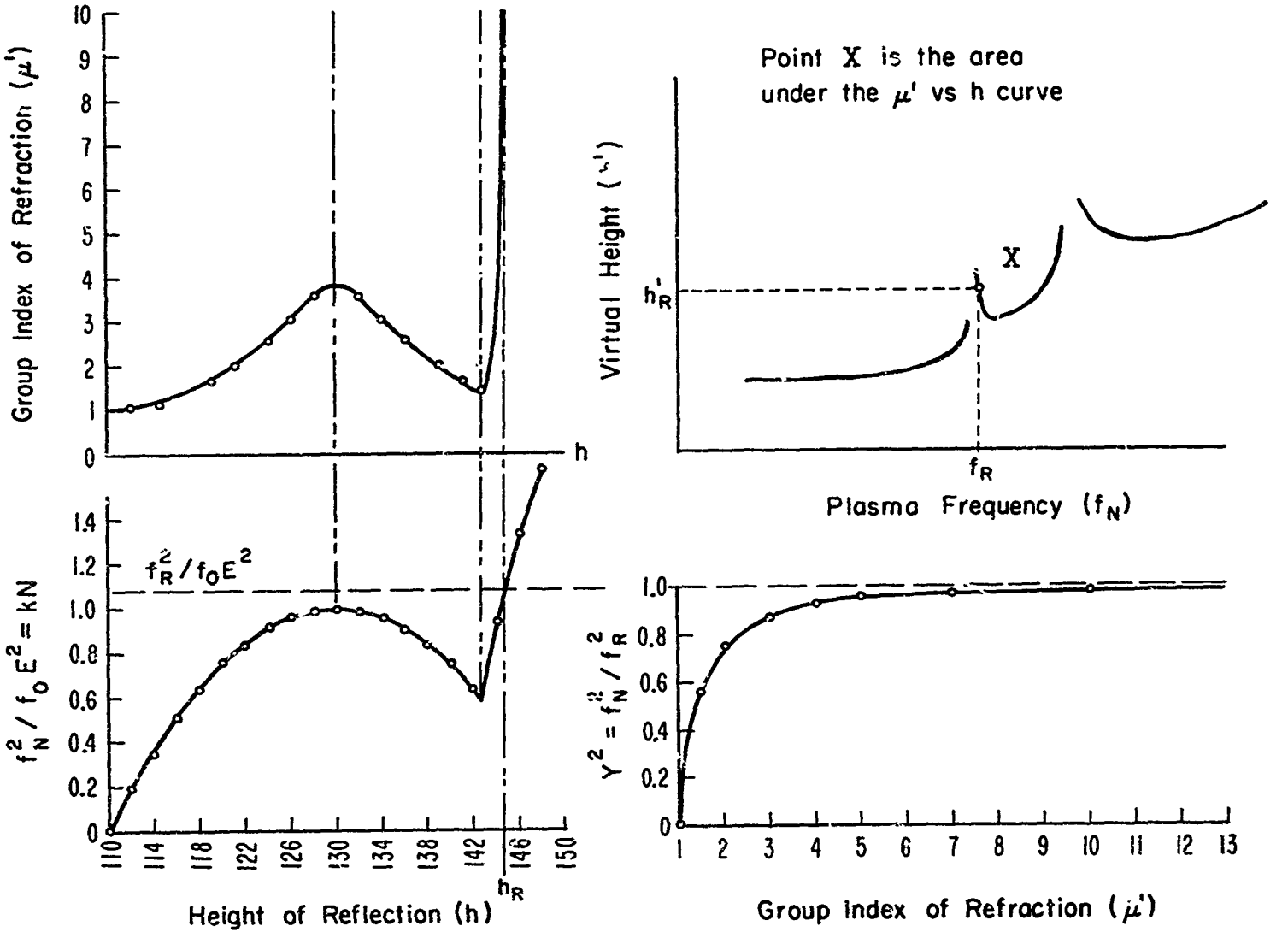


FIGURE 3 GENERATION OF VIRTUAL HEIGHTS

In the program a table of $\mu'$ as a function of $y^2$ (Figure 3, lower right) is stored. For each value of $n_r$, the graph of $\mu'$ (Figure 3, upper left) is generated using the table of $\mu'$ and $y^2$. The virtual height corresponding to $h_r$ is then the area under the $\mu'$ vs h curve (Figure 3, upper left). This procedure gives a virtual-height ionogram (Figure 4) with a minimum of calculations for any tabulated electron-density profile. The virtual-height trace completes the description of the ionosphere except for the absorption factor discussed in detail below. This completes the first half of the program which can, of course, be used as a complete program to generate ionospheric indices, electron-density profiles, and virtual-height ionograms on a worldwide basis from the ITS median prediction coefficients.

The second half of the program is designed to specify the area coverage of a transmitter operating in the decameter wave band. The expected input is virtual-height ionograms describing the ionosphere at selected sample points along the desired azimuth. This input can either be that generated by the first half of the model, or it can be entered separately from data obtained elsewhere. The following simplifying assumptions will be made to derive the raypath:

(1) Horizontal and azimuthal variations in the ionospheric electron-density profiles will be ignored (for each hop; on a multihop path different sample areas are used).

(2) Magnetic-field variations are ignored.

(3) The ionosphere is spherically symmetrical.

With these assumptions the raypath is completely specified by Bouger's rule, which is equivalent to Snell's law for raypaths within a spherically symmetric medium (Figure 5), and is defined by:

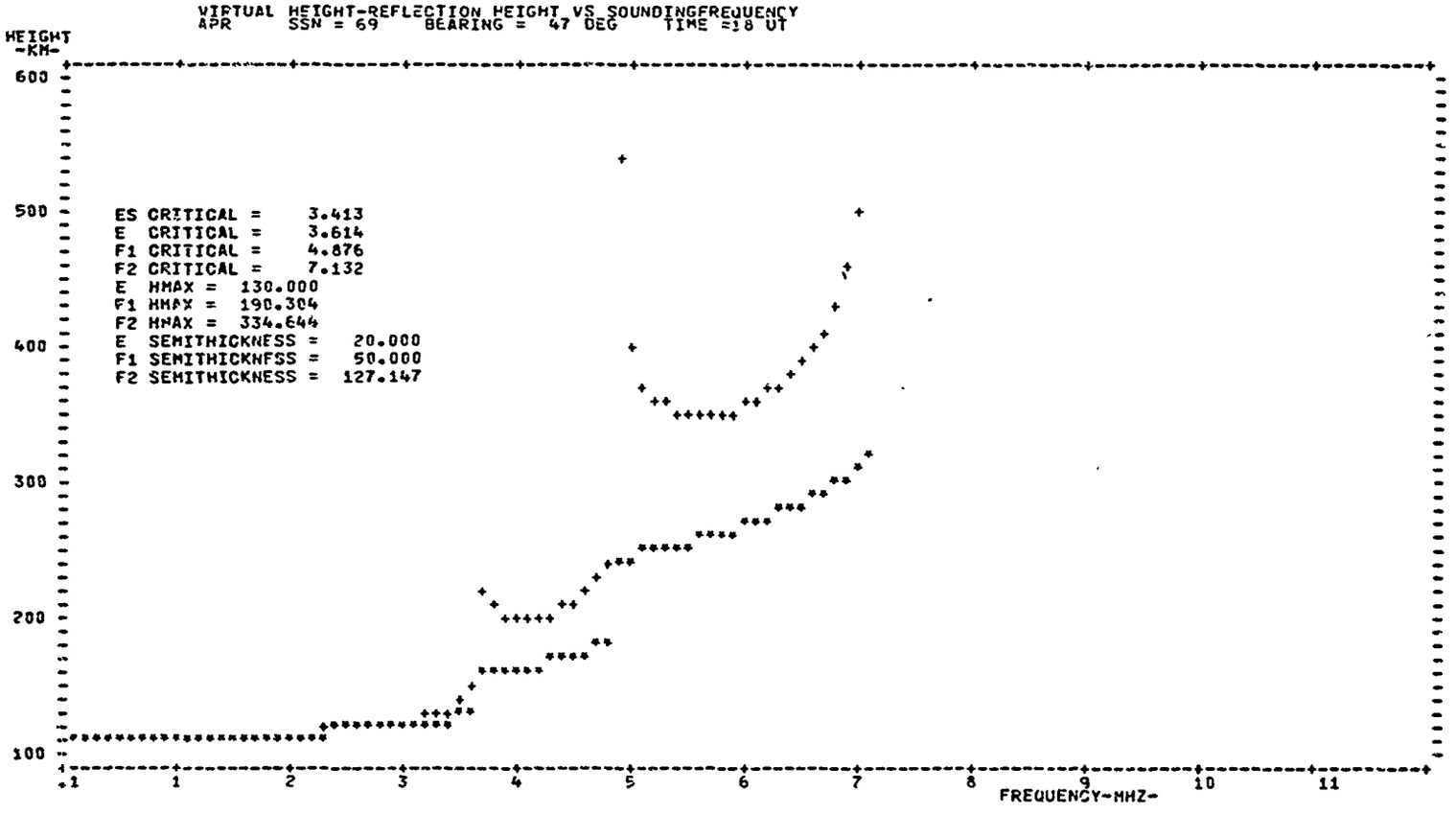


FIGURE 4 VIRTUAL-HEIGHT IONOGRAM

$$\mu r \sin\theta = \text{constant} \tag{3a}$$

or

$$f_o = f_v \sec\phi \tag{3b}$$

where

$\mu$ = Index of refraction

$r$ = Radius from the center to the ray

$\theta$ = Angle between the ray and the normal to the sphere

$\phi$ = Angle between the apparent raypath and the normal to the sphere at the true height of reflection

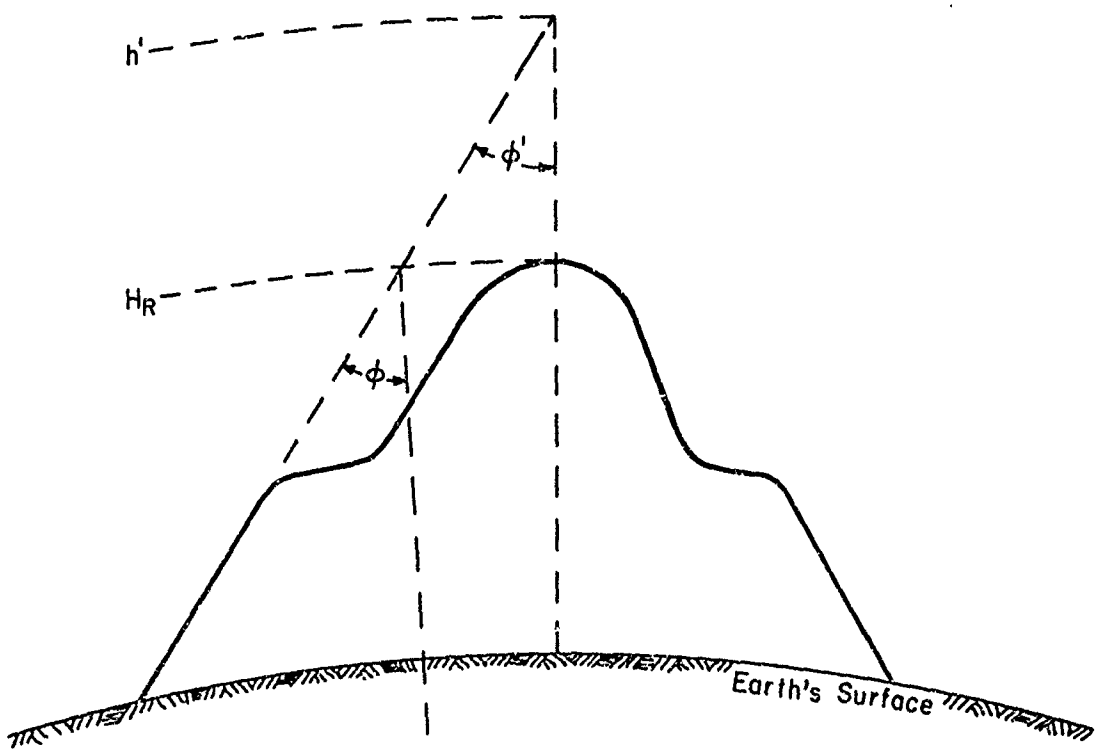


FIGURE 5 RAYPATH GEOMETRY

$$\sin\phi = \frac{\sin\Delta}{1 + h_r/r_e} \tag{4}$$

$\Delta$ = Take-off angle of the ray

$h_r$ = True height of reflection

$r_e$ = Earth's radius.

The model used Eqs. (4) and (3b) to generate Table 1. The first column is the table index. This also corresponds to ten times the vertical sounding frequency--e.g., the 17th row of the table is for a frequency of 1.7 MHz. The second column is the true height of reflection, $h_r$; the third column is the virtual height of reflection, h'; and the columns following are the equivalent oblique operating frequencies of the transmitter for ray paths with corresponding take-off angles--e.g., the column under 0 is for raypaths with a take-off angle of $0^\circ$. Table 1 has a one-degree increment between take-off angles for this example; the increment is arbitrary for the program. When the information contained in Table 1 is plotted in constant-frequency contours of virtual reflection height and distance as in Figure 6, the displayed contours are called reflectrices.[11,12] At each given operating frequency the area coverage is found by interpolating in Table 1 for the desired raypaths. This procedure yields the desired reflectrix for the given frequency in the form of a table of raysets (the first six columns of Table 2). No calculations are necessary at each frequency, since all the desired information is contained in Table 1. For two-hop modes, a table of reflectrix information (as in Table 1) is generated for the second-hop sample area, and at the given operating frequency a table of rayset

## Table 1

## REFLECTRIX INFORMATION

RADIATION ANGLE-OPERATING FREQUENCY TABLE
4PR SSN = 69 BEARING = 47 DEG TIME =18 UT

| I | MT | HP | AFAC | 0 | 1 | 2 | 3 | 4 | 5 | 6 | 7 | 8 | 9 | 10 |
|---|---|---|---|---|---|---|---|---|---|---|---|---|---|---|
| 1 | 112.01 | 112.02 | -27.67 | 0.00 | 0.00 | 0.00 | 0.00 | 0.00 | 0.00 | 0.00 | 0.00 | 0.00 | 0.00 | 0.00 |
| 2 | 112.04 | 112.08 | -21.64 | 1.08 | 1.08 | 1.07 | 1.07 | 1.05 | 1.04 | 1.02 | 1.01 | 0.99 | 0.97 | 0.94 |
| 3 | 112.08 | 112.17 | -18.20 | 1.62 | 1.62 | 1.61 | 1.60 | 1.58 | 1.56 | 1.54 | 1.51 | 1.48 | 1.45 | 1.42 |
| 4 | 112.16 | 112.32 | -15.71 | 2.16 | 2.16 | 2.15 | 2.13 | 2.11 | 2.08 | 2.05 | 2.01 | 1.97 | 1.93 | 1.89 |
| 5 | 112.23 | 112.52 | -13.77 | 2.70 | 2.69 | 2.68 | 2.66 | 2.63 | 2.60 | 2.56 | 2.52 | 2.47 | 2.41 | 2.36 |
| 6 | 112.33 | 112.75 | -12.19 | 3.24 | 3.23 | 3.22 | 3.19 | 3.16 | 3.12 | 3.07 | 3.02 | 2.96 | 2.90 | 2.83 |
| 7 | 112.45 | 113.00 | -10.85 | 3.77 | 3.77 | 3.75 | 3.72 | 3.68 | 3.64 | 3.58 | 3.52 | 3.45 | 3.38 | 3.30 |
| 8 | 112.58 | 113.29 | -9.68 | 4.31 | 4.30 | 4.28 | 4.25 | 4.21 | 4.15 | 4.09 | 4.02 | 3.94 | 3.86 | 3.77 |
| 9 | 112.74 | 114.65 | -8.65 | 4.85 | 4.84 | 4.82 | 4.78 | 4.73 | 4.67 | 4.60 | 4.52 | 4.43 | 4.34 | 4.24 |
| 10 | 112.91 | 114.04 | -7.72 | 5.38 | 5.37 | 5.35 | 5.31 | 5.25 | 5.19 | 5.11 | 5.02 | 4.92 | 4.82 | 4.71 |
| 11 | 113.10 | 114.46 | -6.87 | 5.91 | 5.90 | 5.88 | 5.83 | 5.77 | 5.70 | 5.61 | 5.52 | 5.41 | 5.30 | 5.18 |
| 12 | 113.31 | 114.91 | -6.10 | 6.45 | 6.44 | 6.41 | 6.36 | 6.29 | 6.21 | 6.12 | 6.01 | 5.90 | 5.77 | 5.64 |
| 13 | 113.54 | 115.40 | -5.38 | 6.98 | 6.97 | 6.93 | 6.88 | 6.81 | 6.72 | 6.62 | 6.51 | 6.38 | 6.25 | 6.11 |
| 14 | 113.78 | 115.93 | -4.72 | 7.50 | 7.49 | 7.46 | 7.40 | 7.33 | 7.23 | 7.13 | 7.00 | 6.87 | 6.72 | 6.57 |
| 15 | 114.05 | 116.62 | -4.08 | 8.03 | 8.02 | 7.99 | 7.92 | 7.84 | 7.74 | 7.63 | 7.49 | 7.35 | 7.20 | 7.04 |
| 16 | 114.37 | 117.41 | -3.48 | 8.56 | 8.54 | 8.50 | 8.44 | 8.36 | 8.25 | 8.12 | 7.98 | 7.83 | 7.67 | 7.50 |
| 17 | 114.70 | 118.20 | -2.91 | 9.08 | 9.06 | 9.02 | 8.96 | 8.87 | 8.75 | 8.62 | 8.47 | 8.31 | 8.14 | 7.96 |
| 18 | 115.06 | 119.02 | -2.37 | 9.60 | 9.58 | 9.54 | 9.47 | 9.37 | 9.25 | 9.12 | 8.96 | 8.79 | 8.61 | 8.42 |
| 19 | 115.44 | 119.88 | -1.85 | 10.11 | 10.10 | 10.05 | 9.98 | 9.88 | 9.75 | 9.61 | 9.44 | 9.27 | 9.07 | 8.87 |
| 20 | 115.83 | 120.78 | -1.36 | 10.63 | 10.61 | 10.57 | 10.49 | 10.38 | 10.25 | 10.10 | 9.93 | 9.74 | 9.54 | 9.33 |
| 21 | 116.26 | 122.13 | -0.85 | 11.14 | 11.12 | 11.07 | 10.99 | 10.88 | 10.75 | 10.59 | 10.41 | 10.21 | 10.00 | 9.78 |
| 22 | 116.78 | 123.33 | -0.38 | 11.64 | 11.63 | 11.58 | 11.49 | 11.38 | 11.24 | 11.07 | 10.88 | 10.68 | 10.46 | 10.23 |
| 23 | 117.30 | 124.53 | 0.07 | 12.15 | 12.13 | 12.08 | 11.99 | 11.87 | 11.72 | 11.55 | 11.36 | 11.14 | 10.92 | 10.68 |
| 24 | 117.84 | 125.76 | 0.51 | 12.65 | 12.63 | 12.57 | 12.48 | 12.36 | 12.21 | 12.03 | 11.83 | 11.61 | 11.37 | 11.12 |
| 25 | 118.47 | 127.69 | 0.99 | 13.14 | 13.12 | 13.06 | 12.97 | 12.84 | 12.69 | 12.50 | 12.29 | 12.06 | 11.82 | 11.57 |
| 26 | 119.15 | 129.36 | 1.43 | 13.63 | 13.61 | 13.55 | 13.45 | 13.32 | 13.16 | 12.97 | 12.75 | 12.52 | 12.27 | 12.00 |
| 27 | 119.85 | 131.04 | 1.85 | 14.11 | 14.09 | 14.03 | 13.93 | 13.80 | 13.63 | 13.43 | 13.21 | 12.97 | 12.71 | 12.44 |
| 28 | 120.69 | 133.97 | 2.37 | 14.58 | 14.56 | 14.50 | 14.40 | 14.26 | 14.09 | 13.89 | 13.66 | 13.41 | 13.14 | 12.86 |
| 29 | 121.58 | 136.22 | 2.81 | 15.05 | 15.03 | 14.97 | 14.86 | 14.72 | 14.54 | 14.34 | 14.10 | 13.85 | 13.57 | 13.29 |
| 30 | 122.62 | 140.56 | 3.43 | 15.51 | 15.48 | 15.42 | 15.31 | 15.17 | 14.99 | 14.78 | 14.54 | 14.27 | 13.99 | 13.70 |
| 31 | 123.80 | 143.76 | 3.92 | 15.95 | 15.93 | 15.86 | 15.75 | 15.60 | 15.42 | 15.20 | 14.96 | 14.69 | 14.41 | 14.11 |
| 32 | 125.29 | 150.35 | 4.70 | 16.37 | 16.35 | 16.24 | 16.17 | 16.02 | 15.83 | 15.61 | 15.36 | 15.09 | 14.80 | 14.50 |
| 33 | 127.26 | 161.11 | 5.84 | 16.75 | 16.73 | 16.66 | 16.55 | 16.40 | 16.21 | 15.99 | 15.74 | 15.46 | 15.17 | 14.86 |
| 34 | 131.88 | 231.05 | 12.63 | 16.96 | 16.94 | 16.88 | 16.77 | 16.62 | 16.43 | 16.22 | 15.97 | 15.70 | 15.41 | 15.11 |
| 35 | 153.84 | 216.51 | 9.77 | 16.21 | 16.19 | 16.14 | 16.05 | 15.93 | 15.77 | 15.59 | 15.39 | 15.16 | 14.91 | 14.65 |
| 36 | 154.79 | 207.95 | 4.07 | 16.62 | 16.60 | 16.55 | 16.46 | 16.33 | 16.18 | 15.99 | 15.79 | 15.55 | 15.30 | 15.04 |
| 37 | 155.78 | 204.16 | 1.20 | 17.03 | 17.01 | 16.96 | 16.87 | 16.74 | 16.58 | 16.39 | 16.18 | 15.94 | 15.69 | 15.42 |
| 38 | 156.91 | 203.71 | 0.25 | 17.43 | 17.41 | 17.36 | 17.26 | 17.13 | 16.97 | 16.78 | 16.56 | 16.32 | 16.06 | 15.79 |
| 39 | 158.11 | 204.49 | 0.00 | 17.83 | 17.81 | 17.75 | 17.65 | 17.52 | 17.36 | 17.16 | 16.94 | 16.70 | 16.44 | 16.16 |
| 40 | 159.51 | 206.99 | 0.33 | 18.20 | 18.18 | 18.13 | 18.03 | 17.90 | 17.73 | 17.54 | 17.31 | 17.06 | 16.80 | 16.51 |
| 41 | 161.13 | 212.80 | 1.59 | 18.57 | 18.55 | 18.49 | 18.39 | 18.25 | 18.09 | 17.89 | 17.67 | 17.42 | 17.15 | 16.86 |
| 42 | 163.06 | 220.56 | 3.34 | 18.91 | 18.89 | 18.83 | 18.74 | 18.60 | 18.43 | 18.23 | 18.01 | 17.75 | 17.48 | 17.19 |
| 43 | 165.59 | 232.12 | 6.04 | 19.22 | 19.20 | 19.14 | 19.04 | 18.91 | 18.74 | 18.54 | 18.31 | 18.06 | 17.78 | 17.49 |
| 44 | 171.03 | 316.04 | 29.59 | 13.66 | 19.34 | 19.29 | 19.19 | 19.06 | 18.89 | 18.70 | 18.48 | 18.23 | 17.96 | 17.67 |
| 45 | 217.76 | 331.42 | 18.56 | 17.64 | 17.63 | 17.59 | 17.52 | 17.43 | 17.31 | 17.17 | 17.00 | 16.82 | 16.62 | 16.40 |
| 46 | 218.65 | 313.47 | 11.02 | 18.00 | 17.99 | 17.95 | 17.88 | 17.78 | 17.66 | 17.51 | 17.35 | 17.16 | 16.96 | 16.74 |
| 47 | 219.56 | 304.51 | 7.07 | 18.36 | 18.34 | 18.30 | 18.23 | 18.15 | 18.01 | 17.86 | 17.69 | 17.50 | 17.30 | 17.08 |
| 48 | 220.50 | 299.32 | 4.82 | 18.71 | 18.70 | 18.65 | 18.58 | 18.48 | 18.36 | 18.21 | 18.04 | 17.84 | 17.63 | 17.41 |
| 49 | 221.47 | 295.88 | 3.28 | 19.06 | 19.04 | 19.00 | 18.93 | 18.83 | 18.73 | 18.58 | 18.38 | 18.18 | 17.97 | 17.74 |
| 50 | 222.48 | 293.41 | 2.23 | 19.41 | 19.39 | 19.35 | 19.27 | 19.17 | 19.04 | 18.89 | 18.71 | 18.52 | 18.30 | 18.07 |
| 51 | 223.52 | 291.61 | 1.53 | 19.75 | 19.74 | 19.69 | 19.62 | 19.51 | 19.38 | 19.23 | 19.05 | 18.85 | 18.63 | 18.39 |
| 52 | 224.60 | 290.24 | 1.04 | 20.09 | 20.08 | 20.03 | 19.96 | 19.85 | 19.72 | 19.56 | 19.38 | 19.18 | 18.96 | 18.72 |
| 53 | 225.71 | 289.17 | 0.68 | 20.43 | 20.42 | 20.37 | 20.29 | 20.19 | 20.05 | 19.89 | 19.71 | 19.51 | 19.28 | 19.04 |
| 54 | 226.86 | 288.29 | 0.40 | 20.77 | 20.75 | 20.70 | 20.63 | 20.52 | 20.38 | 20.22 | 20.04 | 19.83 | 19.60 | 19.36 |
| 55 | 228.04 | 287.51 | 0.20 | 21.10 | 21.08 | 21.04 | 20.96 | 20.85 | 20.71 | 20.55 | 20.36 | 20.15 | 19.92 | 19.68 |
| 56 | 229.28 | 287.04 | 0.05 | 21.43 | 21.41 | 21.36 | 21.28 | 21.18 | 21.04 | 20.87 | 20.68 | 20.47 | 20.24 | 19.99 |
| 57 | 230.56 | 286.67 | 0.12 | 21.75 | 21.74 | 21.69 | 21.61 | 21.50 | 21.36 | 21.19 | 21.00 | 20.79 | 20.55 | 20.30 |
| 58 | 231.88 | 300.92 | 0.18 | 22.07 | 22.06 | 22.01 | 21.93 | 21.82 | 21.68 | 21.51 | 21.32 | 21.10 | 20.86 | 20.61 |
| 59 | 233.26 | 303.49 | 0.30 | 22.39 | 22.38 | 22.33 | 22.25 | 22.13 | 21.99 | 21.82 | 21.63 | 21.41 | 21.17 | 20.91 |
| 60 | 234.69 | 306.27 | 0.43 | 22.71 | 22.69 | 22.64 | 22.56 | 22.44 | 22.30 | 22.13 | 21.94 | 21.72 | 21.47 | 21.21 |
| 61 | 236.17 | 309.04 | 0.56 | 23.02 | 23.00 | 22.95 | 22.87 | 22.75 | 22.61 | 22.44 | 22.24 | 22.02 | 21.77 | 21.51 |
| 62 | 237.72 | 312.12 | 0.71 | 23.32 | 23.30 | 23.25 | 23.17 | 23.06 | 22.91 | 22.74 | 22.54 | 22.32 | 22.07 | 21.81 |
| 63 | 239.33 | 315.73 | 0.91 | 23.62 | 23.60 | 23.55 | 23.47 | 23.35 | 23.21 | 23.04 | 22.83 | 22.61 | 22.36 | 22.10 |
| 64 | 241.02 | 319.57 | 1.13 | 23.92 | 23.90 | 23.85 | 23.76 | 23.65 | 23.50 | 23.33 | 23.13 | 22.90 | 22.65 | 22.38 |
| 65 | 242.78 | 323.69 | 1.37 | 24.21 | 24.19 | 24.14 | 24.05 | 23.94 | 23.79 | 23.61 | 23.41 | 23.18 | 22.93 | 22.67 |
| 66 | 244.62 | 328.15 | 1.63 | 24.49 | 24.47 | 24.42 | 24.34 | 24.22 | 24.07 | 23.90 | 23.69 | 23.46 | 23.21 | 22.94 |
| 67 | 246.55 | 333.48 | 1.97 | 24.77 | 24.75 | 24.70 | 24.62 | 24.50 | 24.35 | 24.17 | 23.97 | 23.74 | 23.49 | 23.22 |
| 68 | 248.60 | 339.33 | 2.35 | 25.04 | 25.02 | 24.97 | 24.89 | 24.77 | 24.62 | 24.44 | 24.24 | 24.01 | 23.76 | 23.48 |
| 69 | 250.75 | 345.62 | 2.79 | 25.31 | 25.29 | 25.24 | 25.15 | 25.04 | 24.89 | 24.71 | 24.50 | 24.27 | 24.02 | 23.74 |
| 70 | 253.04 | 352.37 | 3.21 | 25.56 | 25.55 | 25.49 | 25.41 | 25.29 | 25.14 | 24.96 | 24.76 | 24.53 | 24.27 | 24.00 |
| 71 | 255.48 | 361.42 | 3.87 | 25.81 | 25.79 | 25.74 | 25.66 | 25.54 | 25.39 | 25.21 | 25.01 | 24.77 | 24.52 | 24.24 |
| 72 | 258.09 | 371.19 | 4.55 | 26.05 | 26.03 | 25.98 | 25.90 | 25.78 | 25.63 | 25.45 | 25.24 | 25.01 | 24.76 | 24.48 |
| 73 | 260.96 | 382.65 | 5.44 | 26.28 | 26.26 | 26.21 | 26.12 | 26.01 | 25.86 | 25.68 | 25.47 | 25.24 | 24.99 | 24.71 |
| 74 | 264.03 | 394.95 | 6.37 | 26.49 | 26.47 | 26.42 | 26.34 | 26.22 | 26.07 | 25.89 | 25.69 | 25.46 | 25.20 | 24.93 |
| 75 | 267.48 | 410.14 | 7.54 | 26.68 | 26.67 | 26.62 | 26.53 | 26.41 | 26.27 | 26.09 | 25.89 | 25.66 | 25.40 | 25.13 |
| 76 | 271.39 | 427.72 | 8.91 | 26.85 | 26.84 | 26.79 | 26.70 | 26.59 | 26.44 | 26.27 | 26.06 | 25.84 | 25.59 | 25.31 |
| 77 | 275.97 | 450.83 | 10.76 | 27.00 | 26.98 | 26.93 | 26.85 | 26.73 | 26.57 | 26.41 | 26.21 | 25.99 | 25.74 | 25.47 |
| 78 | 281.77 | 497.43 | 14.84 | 27.08 | 27.07 | 27.02 | 26.94 | 26.82 | 26.67 | 26.51 | 26.31 | 26.09 | 25.85 | 25.58 |

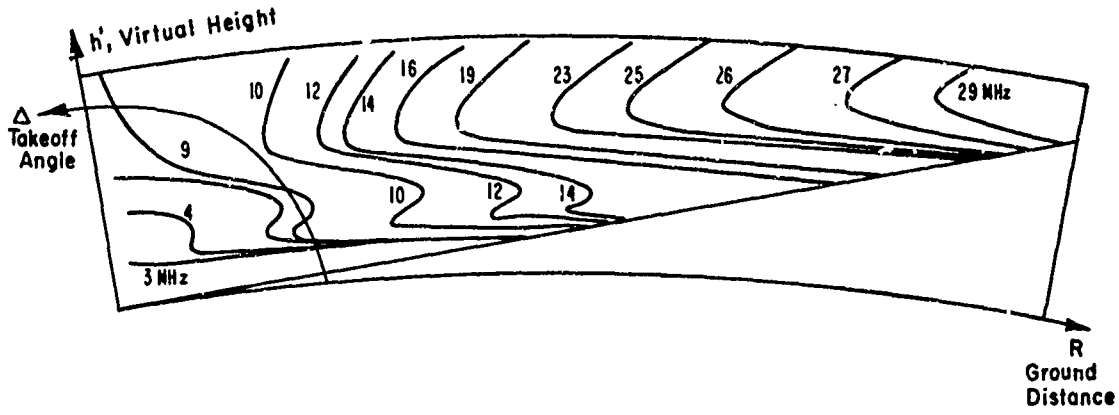


FIGURE 6 REFLECTRICES

information is generated (as in Table 2). The two-hop modes are found by matching the take-off angle of the second hop (DEL1 as in Table 2) with the arrival angle of the first hop (DEL2 in Table 2). Note that there has been no mention of individual layers (E, F1, or F2) since the electron-density profile was generated. The ionosphere is treated as a single region by the program and all possible mode combinations are generated. In order to keep the traditional layer nomenclature, the raypaths are named according to where their equivalent vertical frequencies lie (e.g., below $f_oE$); thus the modes may be E-E, F2-F2, or E-F2, according to the label of each hop. Since the sporadic-E modes are assumed to exist with some degree of probability with reflection at a constant height, the rayset information is the same for each operating frequency and there is no need to generate the equivalent of Table 1 for the $E_s$ modes.

The model then uses the rayset information (Table 2) to add losses to each raypath. For a backscatter radar, the radar range equation is used to generate the signal-to-noise ratio for each raypath. This information is then used to generate the area-coverage plot in Figure 7. The noise information includes atmospheric, galactic, and man-made sources. An additional man-made noise level may be entered as part of the input.

## Table 2

## RAYSET TABLE

RAY SET TABLE
APR SSN = 69 BEARING = 47 DEG TIME =19 UT
FREQUENCY = 15.632MHZ

| TIME | DEL1 | DEL2 | TILT | HITE | GCDNM | ABS | FREE | ANT | BEAM | AREA | BACK | OBF | LOSS | PWR | DBM | RANGE | LAYER | DEV |
|---|---|---|---|---|---|---|---|---|---|---|---|---|---|---|---|---|---|---|
| 18.0 | 0.0 | 0.0 | 0.0 | 141 | 1436 | 25.2 | 249.9 | 0.0 | 9.0 | 14638 | 70.0 | 0.0 | 209 | 64.8 | -145 | 1455 | E | 4.3 |
| 17.2 | 0.6 | 0.6 | 0.0 | 142 | 1367 | 25.2 | 249.1 | 22.2 | 9.0 | 13942 | 69.8 | 0.0 | 209 | 64.8 | -122 | 1386 | E | 4.3 |
| 16.4 | 1.2 | 1.2 | 0.0 | 142 | 1303 | 25.0 | 248.2 | 33.9 | 9.0 | 13299 | 69.6 | 0.0 | 208 | 64.8 | -109 | 1322 | E | 4.4 |
| 15.6 | 1.8 | 1.8 | 0.0 | 143 | 1243 | 24.8 | 247.4 | 40.4 | 9.0 | 12708 | 69.4 | 0.0 | 207 | 64.8 | -102 | 1263 | E | 4.5 |
| 15.0 | 2.4 | 2.4 | 0.0 | 144 | 1190 | 24.5 | 246.7 | 44.7 | 9.0 | 12179 | 69.2 | 0.0 | 207 | 64.8 | -98 | 1210 | E | 5.0 |
| 14.5 | 3.0 | 3.0 | 0.0 | 147 | 1147 | 24.2 | 246.1 | 47.6 | 9.0 | 11766 | 69.0 | 0.0 | 207 | 64.8 | -94 | 1168 | E | 5.4 |
| 14.0 | 3.6 | 3.6 | 0.0 | 151 | 1111 | 23.8 | 245.6 | 49.6 | 9.0 | 11421 | 68.9 | 0.0 | 207 | 64.8 | -92 | 1133 | E | 6.2 |
| 13.8 | 4.2 | 4.2 | 0.0 | 156 | 1093 | 23.3 | 245.3 | 50.8 | 9.0 | 11260 | 68.8 | 0.0 | 207 | 64.8 | -91 | 1116 | E | 7.0 |
| 16.0 | 4.8 | 4.8 | 0.0 | 211 | 1259 | 22.8 | 247.9 | 51.4 | 9.0 | 13084 | 69.5 | 0.0 | 220 | 64.8 | -103 | 1296 | E | 18.4 |
| 15.1 | 5.4 | 5.4 | 0.0 | 205 | 1188 | 22.3 | 246.9 | 51.4 | 9.0 | 12366 | 69.2 | 0.0 | 204 | 64.8 | -88 | 1224 | 1 | 3.8 |
| 14.5 | 6.0 | 6.0 | 0.0 | 204 | 1139 | 21.7 | 246.2 | 50.9 | 9.0 | 11865 | 69.1 | 0.0 | 200 | 64.8 | -84 | 1175 | 1 | 0.8 |
| 14.0 | 6.6 | 6.6 | 0.0 | 204 | 1096 | 21.2 | 245.5 | 49.8 | 9.0 | 11405 | 68.9 | 0.0 | 198 | 64.8 | -83 | 1132 | 1 | 0.1 |
| 13.6 | 7.2 | 7.2 | 0.0 | 205 | 1059 | 20.6 | 245.0 | 48.0 | 9.0 | 11104 | 68.8 | 0.0 | 197 | 64.8 | -84 | 1095 | 1 | 0.4 |
| 13.2 | 7.8 | 7.8 | 0.0 | 208 | 1029 | 20.0 | 244.5 | 45.6 | 9.0 | 10823 | 68.7 | 0.0 | 196 | 64.8 | -87 | 1066 | 1 | 1.8 |
| 13.0 | 8.4 | 8.4 | 0.0 | 214 | 1012 | 19.5 | 244.3 | 42.2 | 9.0 | 10691 | 68.6 | 0.0 | 199 | 64.8 | -92 | 1051 | 1 | 3.7 |
| 13.0 | 9.0 | 9.0 | 0.0 | 222 | 1005 | 18.9 | 244.2 | 37.6 | 9.0 | 10663 | 68.6 | 0.0 | 201 | 64.8 | -99 | 1047 | 1 | 6.8 |
| 14.4 | 9.6 | 9.6 | 0.0 | 266 | 1108 | 18.4 | 246.0 | 31.0 | 9.0 | 11872 | 69.1 | 0.0 | 237 | 64.8 | -141 | 1164 | 1 | 41.5 |
| 15.3 | 10.2 | 11.2 | 0.0 | 299 | 1168 | 17.9 | 247.0 | 20.0 | 9.0 | 12613 | 69.3 | 0.0 | 199 | 64.8 | -114 | 1234 | 2 | 3.5 |
| 14.7 | 10.8 | 10.8 | 0.0 | 295 | 1124 | 17.4 | 246.4 | 0.0 | 9.0 | 12184 | 69.2 | 0.0 | 197 | 64.8 | -132 | 1190 | 2 | 2.0 |
| 14.2 | 11.4 | 11.4 | 0.0 | 294 | 1085 | 16.9 | 245.8 | 12.8 | 9.0 | 11810 | 69.1 | 0.0 | 195 | 64.8 | -117 | 1151 | 2 | 1.0 |
| 13.8 | 12.0 | 12.0 | 0.0 | 293 | 1050 | 16.4 | 245.3 | 25.6 | 9.0 | 11482 | 68.9 | 0.0 | 193 | 64.8 | -103 | 1116 | 2 | 0.5 |
| 13.5 | 12.6 | 12.6 | 0.0 | 293 | 1020 | 15.9 | 244.8 | 32.1 | 9.0 | 11204 | 68.8 | 0.0 | 192 | 64.8 | -95 | 1087 | 2 | 0.2 |
| 13.1 | 13.2 | 13.2 | 0.0 | 293 | 991 | 15.5 | 244.4 | 36.0 | 9.0 | 10947 | 68.7 | 0.0 | 191 | 64.8 | -91 | 1059 | 2 | 0.1 |
| 12.8 | 13.8 | 13.8 | 0.0 | 295 | 966 | 15.1 | 244.0 | 38.4 | 9.0 | 10724 | 68.6 | 0.0 | 190 | 64.8 | -87 | 1035 | 2 | 0.0 |
| 12.5 | 14.4 | 14.4 | 0.0 | 296 | 942 | 14.7 | 243.6 | 39.8 | 9.0 | 10520 | 68.5 | 0.0 | 190 | 64.8 | -85 | 1013 | 2 | 0.1 |
| 12.3 | 15.0 | 15.0 | 0.0 | 298 | 921 | 14.3 | 243.3 | 40.5 | 9.0 | 10346 | 68.5 | 0.0 | 189 | 64.8 | -84 | 993 | 2 | 0.2 |
| 12.1 | 15.6 | 15.6 | 0.0 | 300 | 901 | 13.9 | 243.0 | 40.5 | 9.0 | 10185 | 68.4 | 0.0 | 189 | 64.8 | -83 | 975 | 2 | 0.2 |
| 11.9 | 16.2 | 15.2 | 0.0 | 303 | 883 | 13.6 | 242.7 | 39.9 | 9.0 | 10048 | 68.3 | 0.0 | 188 | 64.8 | -84 | 959 | 2 | 0.5 |
| 11.7 | 16.8 | 15.8 | 0.0 | 306 | 867 | 13.2 | 242.4 | 38.7 | 9.0 | 9933 | 68.3 | 0.0 | 188 | 64.8 | -84 | 945 | 2 | 0.6 |
| 11.5 | 17.4 | 17.4 | 0.0 | 310 | 852 | 12.9 | 242.2 | 37.0 | 9.0 | 9829 | 68.2 | 0.0 | 188 | 64.8 | -86 | 932 | 2 | 0.9 |
| 11.4 | 18.0 | 18.0 | 0.0 | 314 | 839 | 12.6 | 242.0 | 34.7 | 9.0 | 9747 | 68.2 | 0.0 | 188 | 64.8 | -86 | 921 | 2 | 1.2 |
| 11.3 | 18.6 | 18.6 | 0.0 | 318 | 827 | 12.3 | 241.8 | 31.7 | 9.0 | 9687 | 68.2 | 0.0 | 187 | 64.8 | -91 | 913 | 2 | 1.5 |
| 11.2 | 19.2 | 19.2 | 0.0 | 323 | 817 | 12.0 | 241.7 | 28.0 | 9.0 | 9644 | 68.2 | 0.0 | 187 | 64.8 | -95 | 905 | 2 | 1.9 |
| 11.1 | 19.8 | 19.8 | 0.0 | 329 | 808 | 11.7 | 241.6 | 23.2 | 9.0 | 9623 | 68.2 | 0.0 | 188 | 64.8 | -100 | 900 | 2 | 2.4 |
| 11.1 | 20.4 | 20.4 | 0.0 | 336 | 803 | 11.5 | 241.5 | 17.0 | 9.0 | 9637 | 68.2 | 0.0 | 188 | 64.8 | -106 | 898 | 2 | 3.0 |
| 11.1 | 21.0 | 21.0 | 0.0 | 344 | 798 | 11.2 | 241.5 | 8.5 | 9.0 | 9675 | 68.2 | 0.0 | 188 | 64.8 | -115 | 898 | 2 | 3.7 |
| 11.1 | 21.6 | 21.6 | 0.0 | 352 | 796 | 11.0 | 241.6 | 0.0 | 9.0 | 9734 | 68.2 | 0.0 | 189 | 64.8 | -124 | 900 | 2 | 4.4 |
| 11.2 | 22.2 | 22.2 | 0.0 | 364 | 799 | 10.7 | 241.7 | 0.0 | 9.0 | 9875 | 68.3 | 0.0 | 190 | 64.8 | -135 | 909 | 2 | 5.9 |
| 11.4 | 22.8 | 22.8 | 0.0 | 378 | 806 | 10.5 | 242.0 | 0.0 | 9.0 | 10064 | 68.3 | 0.0 | 192 | 64.8 | -127 | 922 | 2 | 7.4 |
| 11.6 | 23.4 | 23.4 | 0.0 | 394 | 815 | 10.3 | 242.3 | 0.0 | 9.0 | 10298 | 68.4 | 0.0 | 193 | 64.8 | -128 | 939 | 2 | 9.0 |
| 12.0 | 24.0 | 24.0 | 0.0 | 414 | 832 | 10.1 | 242.8 | 0.9 | 9.0 | 10639 | 68.6 | 0.0 | 196 | 64.8 | -130 | 966 | 2 | 11.6 |
| 12.5 | 24.6 | 24.6 | 0.0 | 442 | 859 | 9.9 | 243.5 | 1.2 | 9.0 | 11134 | 68.8 | 0.0 | 200 | 64.8 | -134 | 1006 | 2 | 15.1 |
| 13.8 | 25.2 | 25.2 | 0.0 | 503 | 937 | 9.7 | 245.2 | 0.0 | 9.0 | 12365 | 69.2 | 0.0 | 218 | 64.8 | -153 | 1112 | 2 | 32.0 |

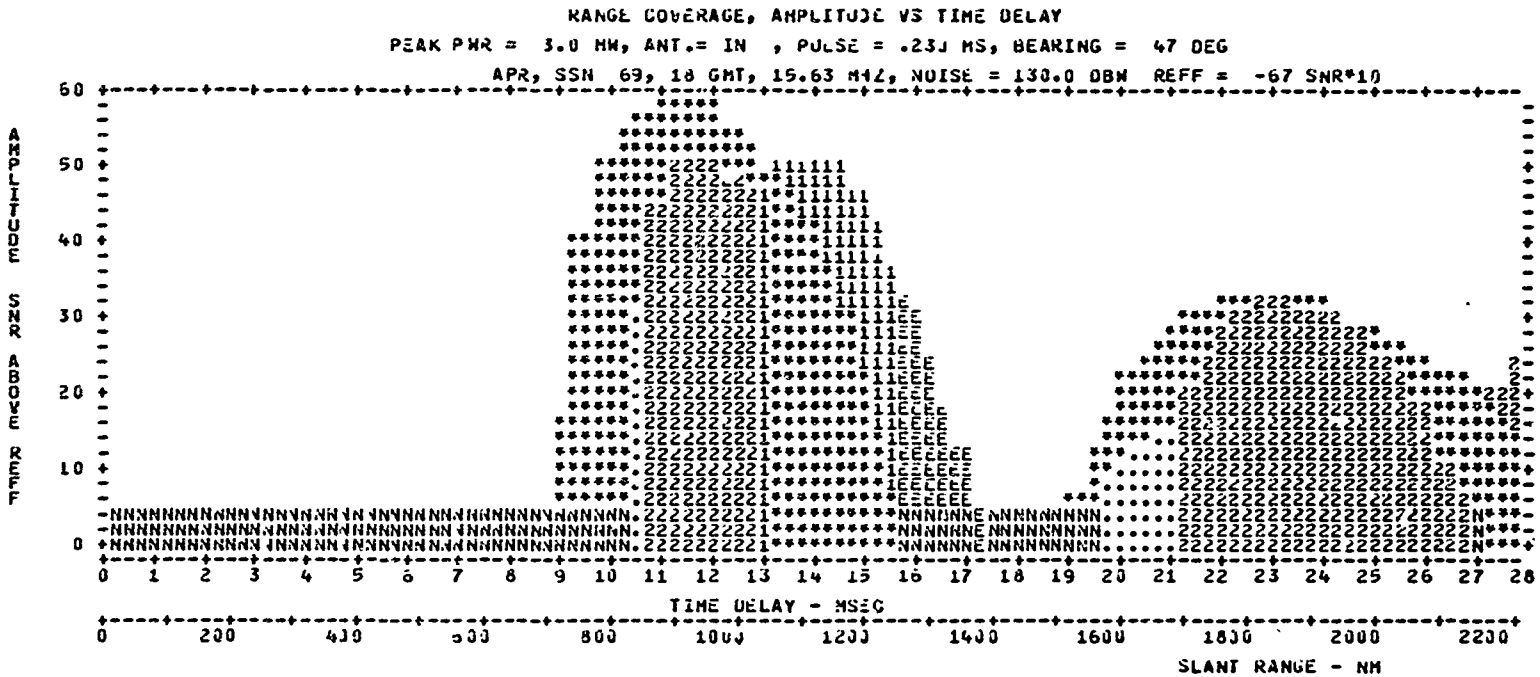


FIGURE 7 BACKSCATTER AMPLITUDES

The losses are those as calculated by Lucas and Haydon[5] with the addition of sporadic-E losses and the deviative and nondeviative loss factor. The sporadic-E losses are reflection losses for modes reflected from the $E_s$ layer and obscuration losses for raypaths penetrating the $E_s$ layer. The losses depend on the probability of a sporadic-E mode existing at the given operating frequency and at the given take-off angle, and is defined by

$$P = \text{Nor}\left(\frac{f - f_s}{\sigma}\right) \tag{5}$$

where

Nor indicates the normal distribution

$f$ = Operating frequency

$f_s$ = Median MUF for the given take-off angle

$\sigma$ = Standard deviation of $f_oE_s$.

The reflection loss is then

$$L_R = 8.91(P)^{-0.7} \tag{6}$$

and the obscuration loss is

$$L_o = 10 \log_{10}(1 - P^2) \quad . \tag{7}$$

The ionospheric losses are based on the absorption losses for D- and E-region absorption of Lucas and Haydon.[5]

The absorption loss in the quasi-longitudinal approximation (Q.L.) is

$$L(f_o) = \left[\frac{L(f_v)(f_v - f_e)}{f_v - f_e}\right] \sec\phi \qquad (8)$$

where

$L(f_o)$ = Absorption for the oblique path with operating frequency f

$L(f_v)$ = Absorption for vertical paths with operating frequency $f_v$

$f_e$ = Longitudinal component of the electron gyrofrequency

$\phi$ = Angle of incidence of the ray at the absorbing region (approximately 100 km).

The term in brackets in Eq. (8) is that fitted by Laitinen and Haydon for both vertical and oblique F-layer paths.[13] Since the data did not include frequencies below 3 MHz, the equation was modified by Lucas and Haydon[5] to

$$L_A = \left[\frac{677.2}{(f + f_h)^{1.98} + 10.2}\right] \sec\phi \quad . \qquad (9)$$

An additional loss factor for E-layer modes has been derived:

$$L_E = 1.359 - 19.841 \log_{10}\left(\frac{f_e}{f_o}\right) \qquad (10)$$

where

$f_e$ = Median MUF for the E layer at the given elevation angle

$f_o$ = Operating frequency.

An additional loss term is now included that takes into account the deviative absorption effects of the higher layers (of most importance for high-angle rays). The theoretical loss is

$$L_v = \int_{\substack{\text{ray} \\ \text{path}}} k \chi \, dz \tag{11}$$

where

$k$ = Propagation constant in free space

$n = \mu - i\chi$ = Refractive index .

Neglecting magnetic-field effects this is

$$I_v = \frac{\nu}{c}(h' - h_p) \tag{12}$$

where

$\nu$ = Collision frequency

$c$ = Speed of light

$h'$ = Virtual height

$h_p$ = Phase height.

In order to obtain an expression that is easily calculated and behaves as Eq. (10), we approximate the bracketed term in Eq. 8 with

$$[\ ] = A(f_v)(h' - h_x) \tag{13}$$

where

$h'$ = Virtual height

$h_r$ = True reflection height

$A(f_v)$ = An empirical fit to the absorption using Eq. (13).

The first column of Table 1 is the index corresponding to ten times the vertical frequency; the second column is the true height of reflection, $h_r$; and the third column is the virtual height, $h'$. The fourth column is the loss term to be added to the losses calculated by Lucas and Haydon[5] [Eq. (9)]--e.g., the sum of Eqs. (10) and (13). In the program $A(f_v)$ is now a given constant value for the E region, the E-F1 cusp, the F1 region, the F1-F2 cusp, and the F2 region. In addition, it is optional to modify this term by any constant multiplication factor (and thus eliminate it entirely if so desired). This representation is, of course, an interim step until the completion of a world map of $A(f_v)$.

## III DATA ANALYSIS

The model as described above can be used with the median ionospheric-index maps as a tool to predict the long-term performance of HF radar and communication systems. The use of the model as a tool to analyze and update the predicted median data will now be described. Assumed available at the beginning of the analysis are the median ionospheric predictions for the month, including the virtual-height ionogram (Figure 4), the expected backscatter amplitude versus range (Figure 7), and the antenna pattern. For this system the antenna is composed of two horizontal rows of elements stacked two high. The antenna patterns resulting from feeding these two rows inphase and antiphase are shown in

Figure 8. A scattering coefficient of $\sigma^{o}$ = -17 dB was used to describe the sea scattering properties of the return.

The model parameters that are varied are those relating to electron-density distribution--the critical frequencies; heights of maximum ionization and semi-thicknesses of the E, F1, and F2-layers; and the critical frequency and height of reflection of the $E_s$ layer. The entire electron-density profile on the entire h′ ionograms can be modified

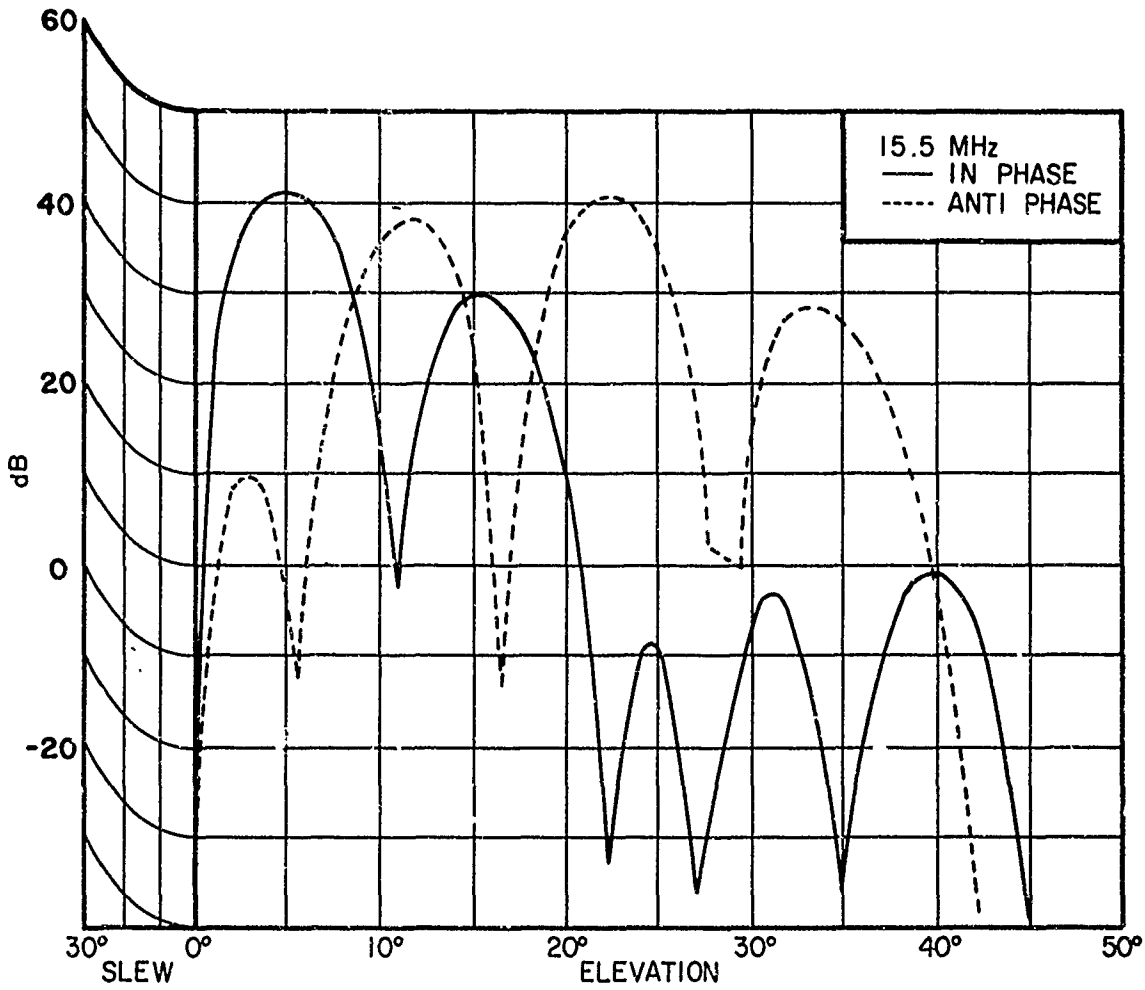


FIGURE 8 ANTENNA TRANSMIT-RECEIVE GAIN PRODUCT GIVEN AS A FUNCTION OF RADIATION ANGLES

directly, but it is easier to consider only the smaller number of indices in a first attempt at describing the actual ionosphere.

A one-frequency backscatter sounding is sufficient to sample all useful heights in the ionosphere; but to determine the ion-height profile, one must be able to identify the ground range(s), R, or radiation angles that correspond to each virtual range, $R'$. Positionable radiation-angle directivity would provide an excellent method for coupling R and $R'$. However, in this exercise the tools available are limited to two multi-lobed antenna-radiation-angle patterns as shown in Figure 8 and a chart for the illuminated region as shown in Figure 9. When the electron density versus height is a smooth monotonic function, the antenna lobe structure such as shown in Figure 8 enables one to easily identify $R'$ values with radiation angles and then compute R values and heights. Hence a more complex ionosphere has been chosen for illustration.

The backscatter level plotted against time delay or range is given in Figures 10 and 11. These levels were obtained by coherently processing for about 0.2 s and then averaging all samples for one minute. This procedure provides a sounding with a good signal-to-noise ratio. Figure 10 was made using the in-phase antenna configuration; there is no obvious antenna lobe structure in the in-phase return; meteor-caused returns can be seen out to 200 nmi; a small hump between 250 and 650 nmi is identified as caused by sporadic E; the major return between 750 and 1600 nmi appears to be from several one-hop paths that have washed-out antenna lobe structure. The amplitude-versus-range pattern shown in Figure 11 is that from the anti-phase antenna element feed. In it, a peak at 900 nmi, a valley at about 1000, and another peak at 1220 are judged to be due to the antenna pattern. Using Figure 8 one can calculate:

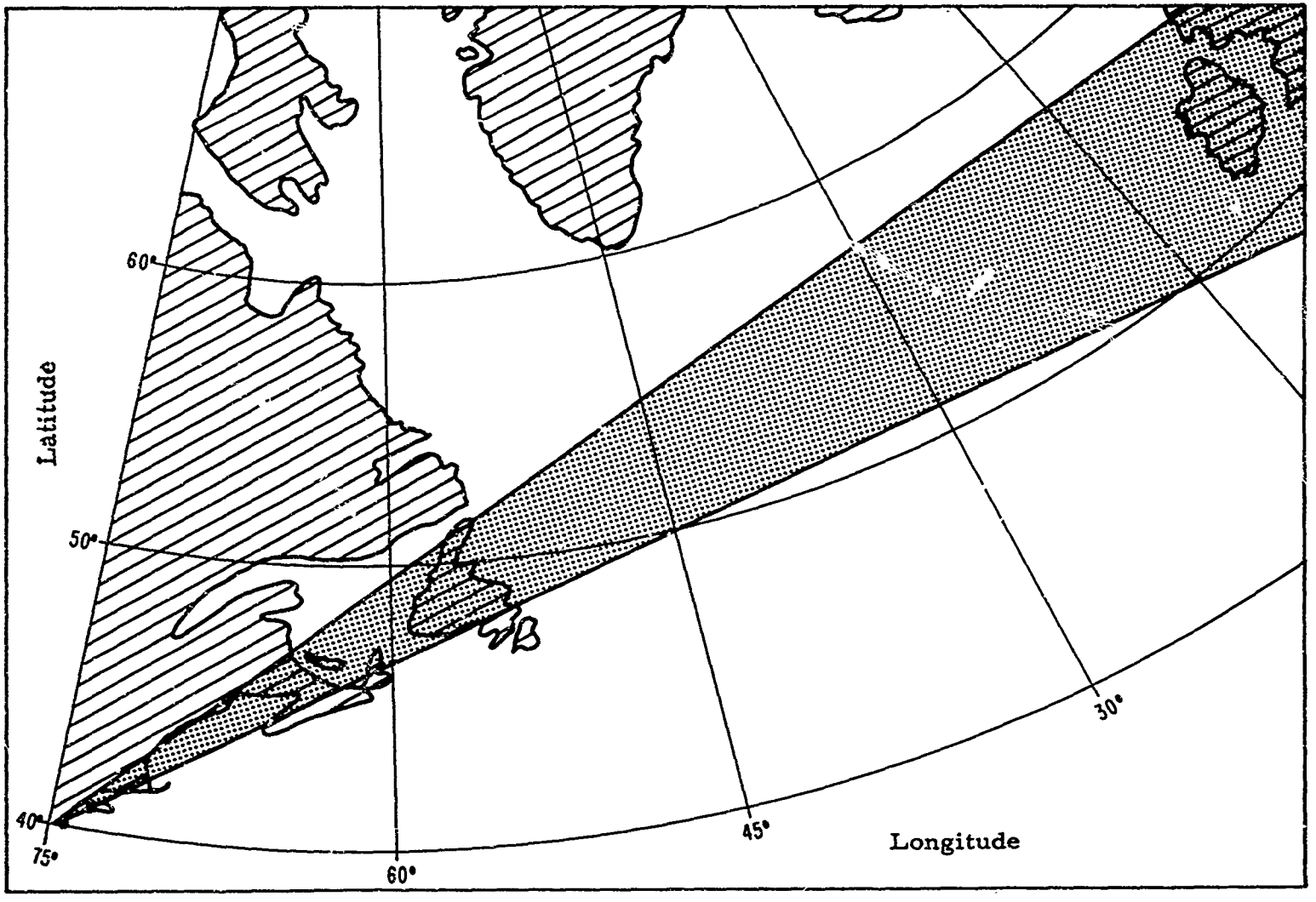


FIGURE 9 GEOGRAPHIC AREA FOR RADAR SAMPLE

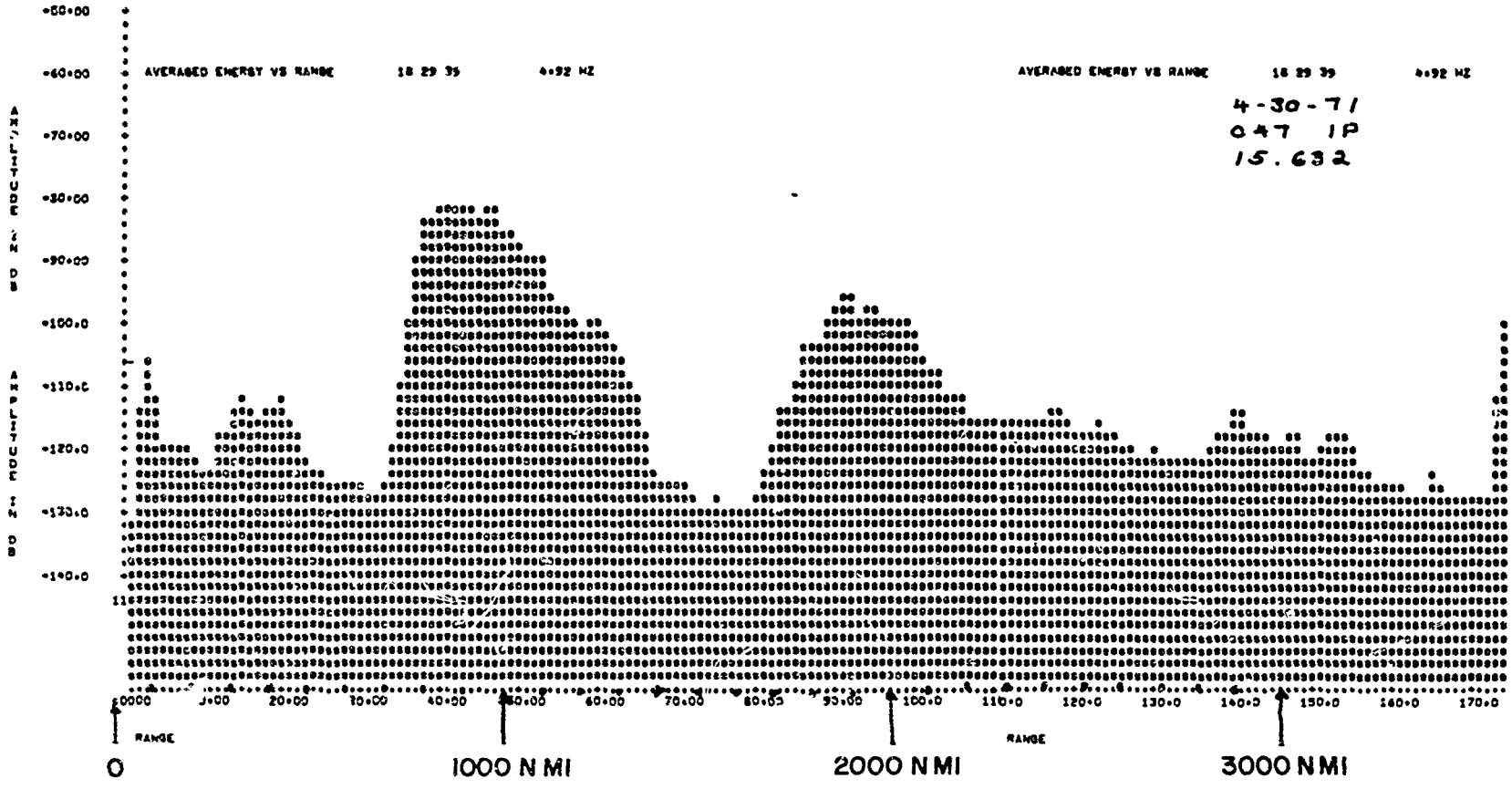


FIGURE 10 RADAR RETURN, IN-PHASE ANTENNA PATTERN

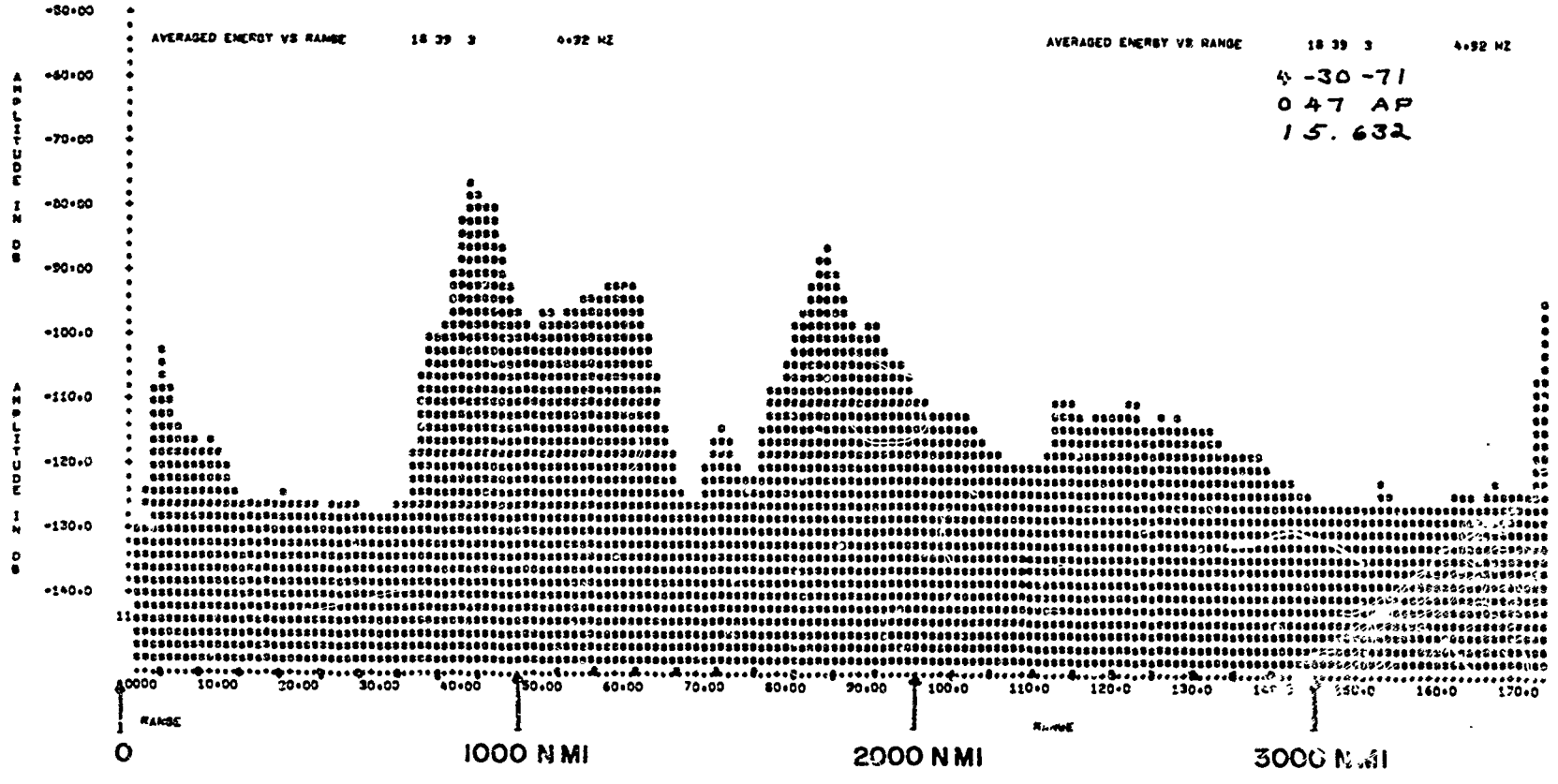


FIGURE 11 RADAR RETURN, ANTIPHASE ANTENNA PATTERN

| Virtual Range (nmi) | Radiation Angle (deg) |
|---|---|
| 900 | 22 |
| 1010 | 16 |
| 1220 | 12 |

These values are approximate and incomplete since they cover but part of the F-region.

A detailed Doppler analysis can aid in path identification. Figure 12 shows such analysis as 6-dB spaced amplitude contours. The upper plot is for the in-phase and the lower for antiphase antenna feed; the ordinate is in Hertz and the abscissa, R′, in hundreds of nmi. The Doppler from sea returns at this frequency is at about ±0.4 Hz and the peak pairs with 0.8-Hz spacing are evident. Land returns are also seen at a zero Doppler. Low-level returns via sporadic E are identifiable between 200 and 600 nmi. The in-phase plot shows evidence of more than one path with a multiplicity of peaks. The antiphase plot tends to support the prior tabulation; further, the minimum in the sea return at R′ = 1180 nmi can be taken as identifying the widest part of Newfoundland at R = 1200 nmi. To better unravel the in-phase plot it was reanalyzed with an expansion of the Doppler scale, and this is shown in Figure 13. The points marked X are the land-range estimates of equidistance from the strait between Nova Scotia and Newfoundland. The center of the strait is at R = 900 nmi and for R′ the estimates are 945 and 985 nmi. Sporadic E is difficult to identify within the larger returns, but since it is evident at the shorter ranges it is probably a contributor to the in-phase returns.

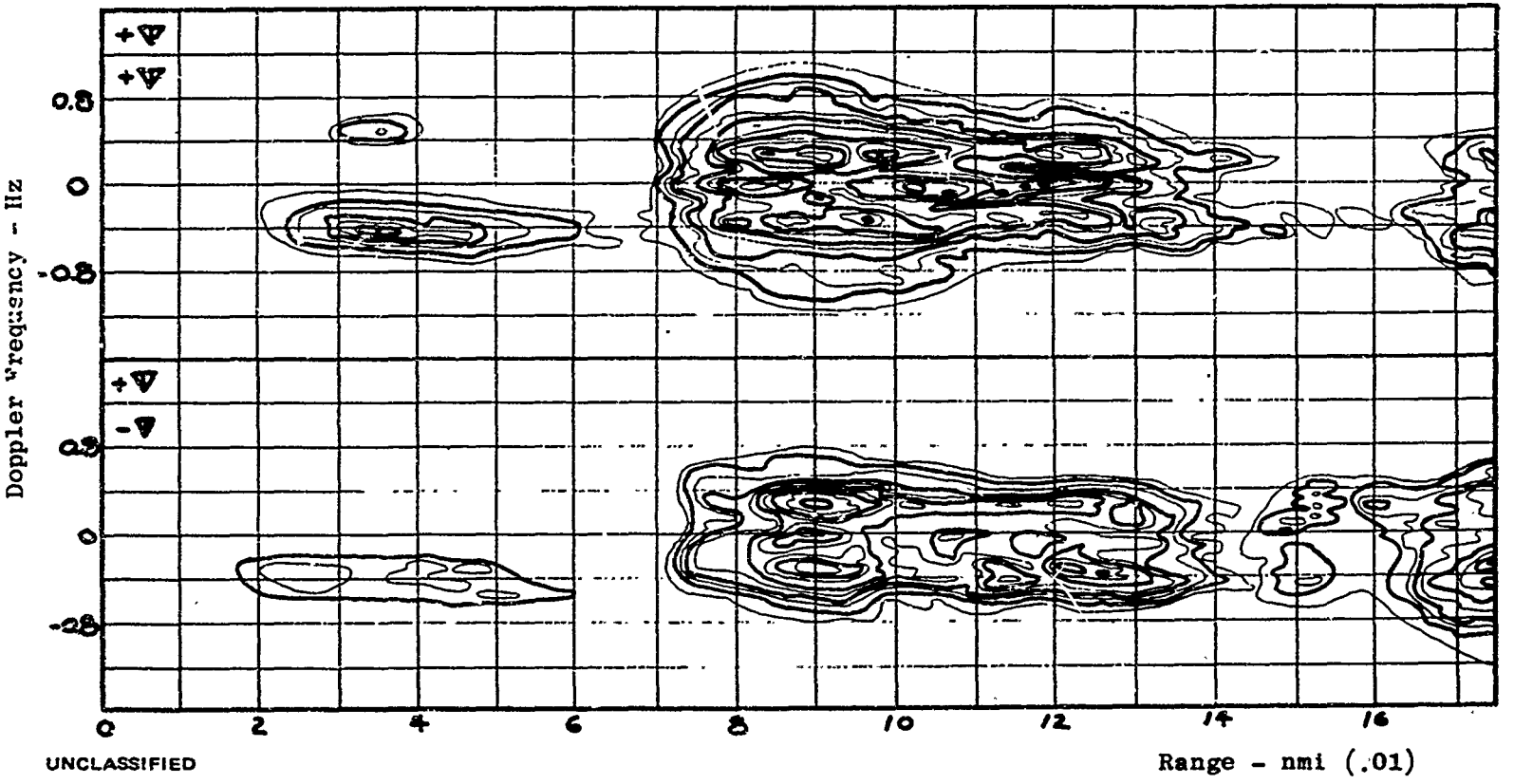


FIGURE 12 DOPPLER ANALYSIS

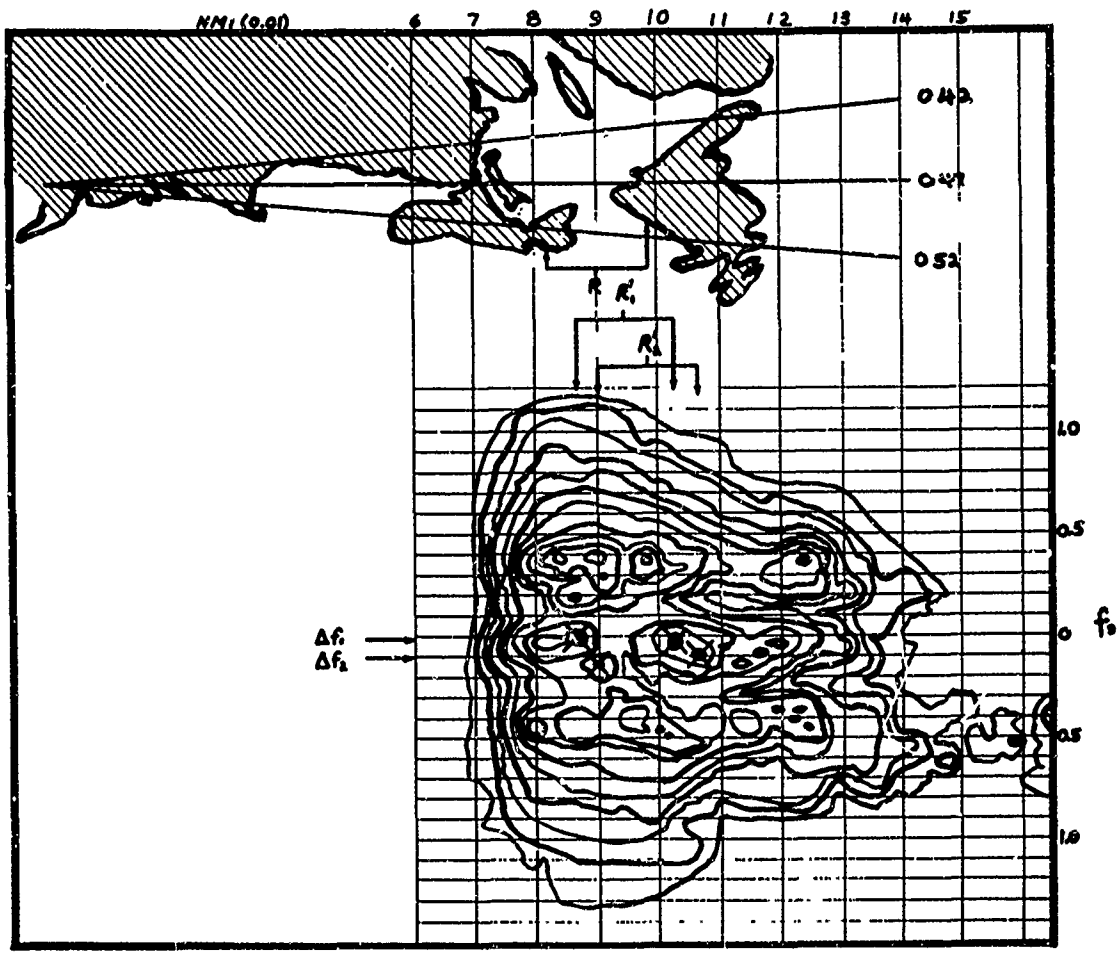


FIGURE 13 DOPPLER ANALYSIS EXPANDED

In summation, the transmission-path description should fit:

| | R(nmi) | $R'_1$(nmi) | $R'_2$(nmi) |
|---|---|---|---|
| Observed | 900 | 945 | 985 |
| Predicted | 900 | Not seen | 982 |
| Observed | 1120 | | 1180 |
| Predicted | 1120 | | 1184 |

in addition to the prior table. Of course the entire shape of the earth returns predicted from the deduced ionosphere should fit the observations. In this particular case the use of a constant-scattering coefficient $\sigma^{o} = -17$ dB can cause some amplitude error. All of the water illuminated may not have possessed this large a scattering coefficient and the land very probably did not.

It is hoped that this exercise has shown the utility of using earth features--here, the Doppler distinctiveness of land and sea echoes for path checkpoints. This work was done with an azimuthal beamwidth of $10^{o}$, one beam position, and a receiver bandwidth of 1.5 kHz. Employing wider bandwidth could considerably increase the accuracy of check-point location.

The model was used to generate median predictions for the month of April. These were compared to the observed values taken on April 30, 1971, and revisions were made to the median predicted ionogram to improve the comparison with the measured backscatter. Tables 1 and 2, and Figures 14, 15, and 16 show the results of running the revised ionosphere. Figure 15, the in-phase return, shows the same shape as measured return, Figure 10. The mode structure, showing combinations of E, $E_s$, F1, and F2 modes, eliminates the smooth antenna pattern from the backscatter. Figure 16, the antiphase return, however, shows the effects of the antenna pattern because the return is now dominated by the F2-layer. The final check on the analysis is to compare the derived ionogram, Figure 17, with soundings taken near the midpath with an ionosonde.

Figure 17 shows this check against a vertical-sounder observation near Boston that is near the actual area of reflection. The "adjusted" ionogram from the one-frequency backscatter observations is very close to that measured except for the F1-F2 cusp region. This does

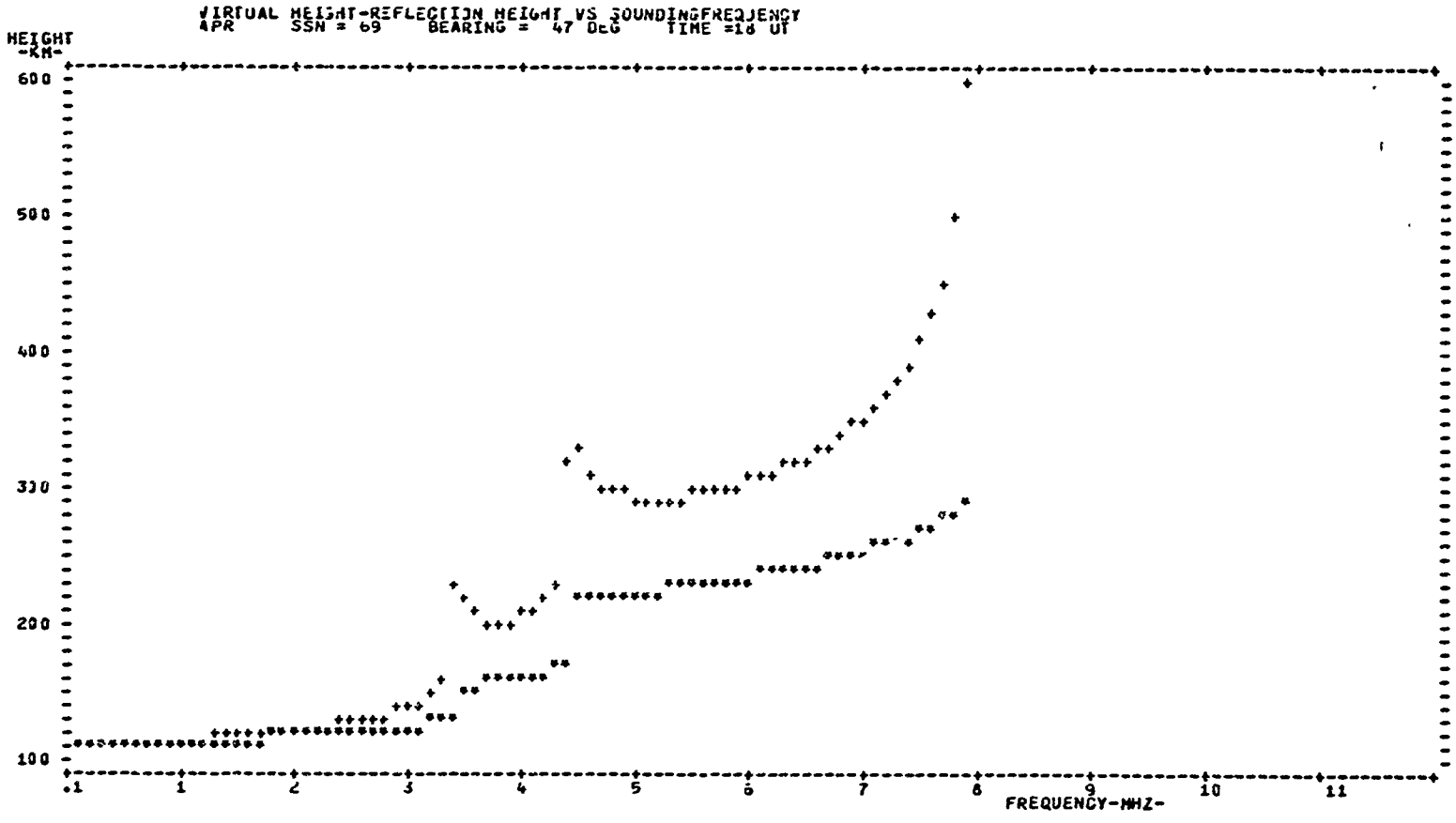


FIGURE 14 ADJUSTED IONOGRAM

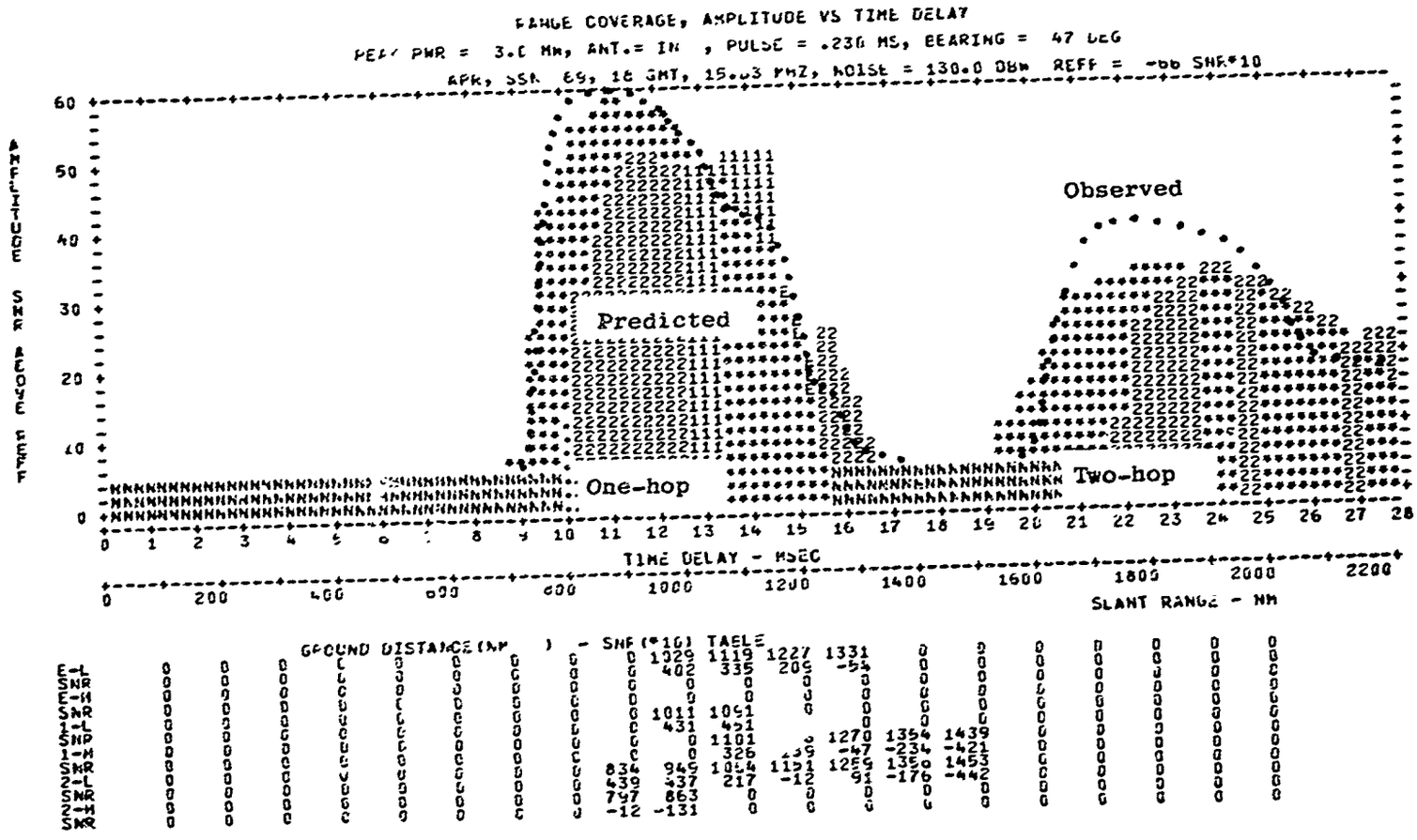


FIGURE 15 ADJUSTED BACKSCATTER-AMPLITUDES IN-PHASE ANTENNA PATTERN

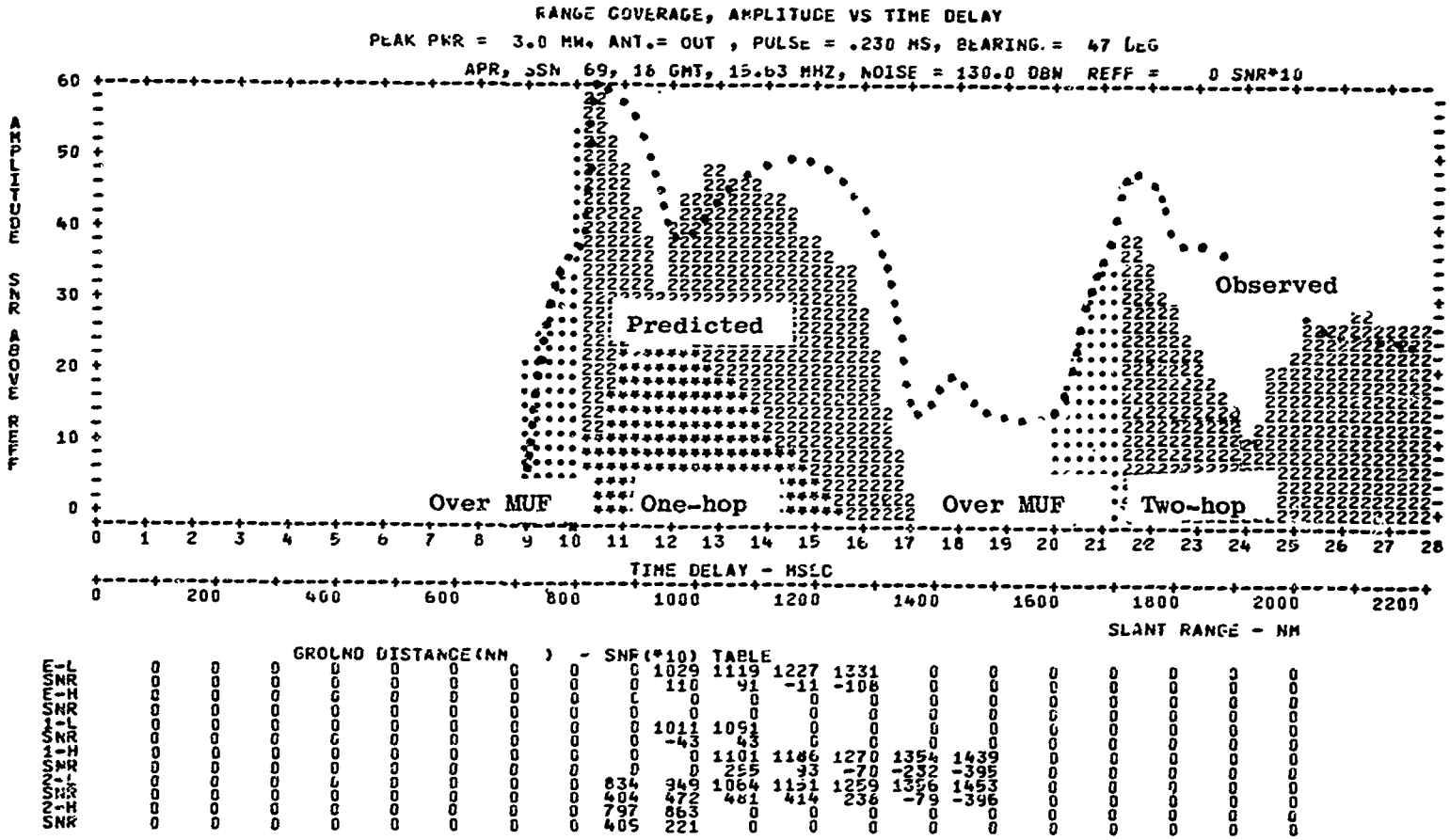


FIGURE 16 ADJUSTED BACKSCATTER-AMPLITUDES ANTIPHASE ANTENNA PATTERN

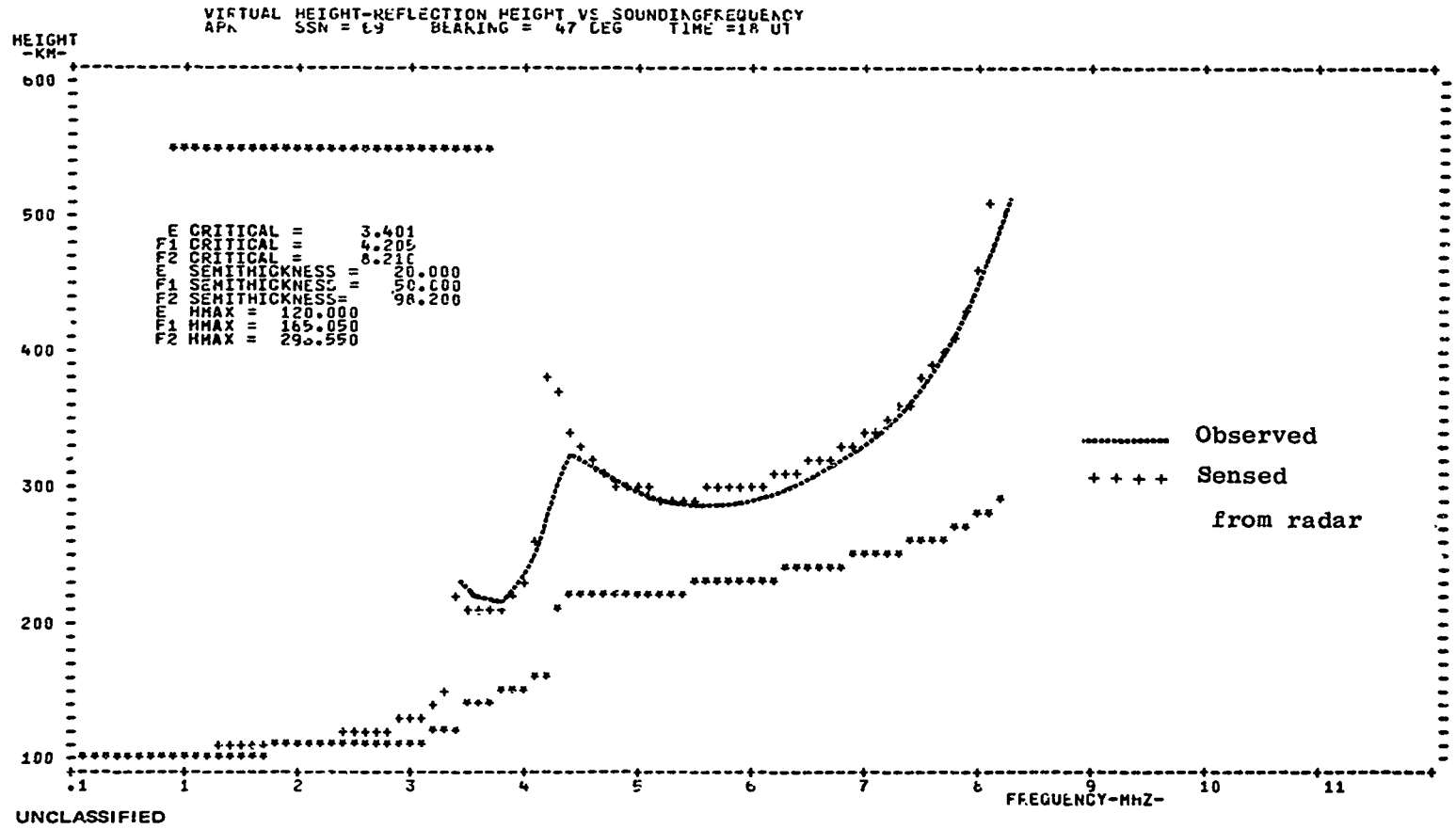


FIGURE 17 ADJUSTED REMOTE IONOSPHERE FROM BACKSCATTER CHECKED AGAINST ACTUAL OBSERVATION

not affect the predicted backscatter to any extent because these rays are highly absorbed when the deviative absorption is used. The remote ionosphere has been adequately sensed using one-frequency backscatter data and two antenna beam positions.

The model described in this paper is a versatile tool that can be used in the description of radar and communication systems that use the ionosphere as a transmitting medium. The complexity of the ionospheric description is intermediate between the simple four-layer models[5,6] and full ray-trace programs. It is constantly being used to predict and analyze observed data. Immediate goals include the construction of methods to improve the merging of the individual E, F1, and F2-layers (e.g., to determine when a cusp is really present), and to improve the deviative absorption factors.

## Appendix

### NUMERICAL MAPS OF $f_oF1$

Reference 9 describes the analysis of $f_oF1$ values for the period January 1954 through December 1966. One result of that analysis is a quadradic fit of $f_oF1$ to the cosine of the sun's zenith angle and a linear fit to sunspot number for each month, defined as follows:

$$f_oF1 = (A + U \cdot R) + (B + V \cdot R) \cos(z) + (C + W \cdot R) \cos^2(z) \qquad (1)$$

where

R = Sunspot number

z = Sun's zenith angle

A, U, B, V, C, and W = Coefficients derived by a least squares fit to the data.

Equation (1) is to be used as long as $Z \leq Z_{max}$ where $Z_{max}$ is given by a linear fit to the cosine of the Rawer modified magnetic dip angle and the sunspot number for each month, as follows:

$$Z_{max} = (D + X \cdot R) + (E + Y \cdot R) \cos (x)$$

where

R = Sunspot number

x = Rawer modified magnetic dip angle

D, X, E and Y = Coefficients derived by a least-squares fit to the data.

## REFERENCES


1. D. L. Lucas, J. M. Headrick, and G. W. Haydon, "HF Radar Environment Synthesis (U)," Proceedings of the OHD Technical Review Meeting of 23-25 October 1968, Vol. II, SRI-8-1244, Stanford Research Institute, Menlo Park, Calif. (November 1968), Limited distribution report.

2. D. L. Lucas et al., "Modeling OHD Radars-Observations and Predictions (U)," Proceedings of the OHD Technical Review Meeting of 11-12 December 1969, Vol. I, SRI-9-1221, Stanford Research Institute, Menlo Park, Calif. (December 1969), Limited distribution report.

3. J. M. Headrick, et al., "Virtual Path Tracing for HF Radar Including an Ionospheric Model," NRL Memo Report 2226, Naval Research Laboratory, Washington, D.C., UNCLASSIFIED. March 29, 1971.

4. W. B. Jones and R. M. Gallet, "Methods for Applying Numerical Maps of Ionospheric Characteristics," J. Res. NBS 66D, No. 6, pp. 649-662 (November-December 1962), UNCLASSIFIED.

5. D. L. Lucas et al., "Predicting Statistical Performance Indexes for High Frequency Telecommunications Systems," ESSA Technical Report, IER-ITSA-1, Environmental Sciences Services Administration, Boulder Colo. (1966), UNCLASSIFIED.

(Page 34 is blank)


6. A. F. Barghausen et al., "Predicting Long-Term Operational Parameters of High-Frequency Sky-Wave Telecommunication Systems, "ESSA Technical Report ERL 110-ITS 78, Environmental Sciences Services Administration, Boulder, Colo. (May 1969), UNCLASSIFIED.

7. W. B. Jones and D. L. Obitts, "1971 Global Representation of Annual and Solar Cycle Variation of $f_oF2$ Monthly Median 1954-1958," OT/ITS Telecom. Research Report 3 (U.S. Government Printing Office Washington, D.C.), UNCLASSIFIED.

8. M. Leftin, S. M. Ostrow, and F. G. Stewart, "Numerical Maps of $f_oE_s$ for Solar Cycle Minimum and Maximum," ESSA Technical Report ERL 73-ITS 63, Environmental Sciences Services Administration, Boulder, Colo. (1968), UNCLASSIFIED.

9. D. H. Zacharisen et al., "Numerical Maps of Monthly Median $f_oF1$ and Maximum Solar Zenith Angle of $f_oF1$ Occurrence," to be published, UNCLASSIFIED.

10. W. B. Jones and F. G. Stewart, "A Numeric Method for Global Mapping of Plasma Frequency," Radio Science, Vol. 5, No. 5 (May 1970), UNCLASSIFIED.

11. P. Lejay and Lepechinsky, "Field Intensity at the Receiver as a Function of Distance," Nature (Lond), 165, 306, 1950.

12. T. A. Croft, "HF Radio Focusing Caused by the Electron Distribution Between Ionospheric Layers," J. Geophys. Res., Vol. 2, No. 9 (May 1967), UNCLASSIFIED.

13. P. O. Laitinen and G. W. Haydon "Analysis and Prediction of Sky-Wave Field Intensities in the High-Frequency Band," Technical Report No. 9, Revised (RPU203), U.S. Army Signal Radio Propagation Agency, Fort Monmouth, N.J., UNCLASSIFIED.